The Diurnal Cycle of Rainfall and the Convectively Coupled Equatorial Waves over the Maritime Continent

NAOKO SAKAEDA

School of Meteorology, University of Oklahoma, Norman, Oklahoma

GEORGE KILADIS AND JULIANA DIAS

NOAA/Earth System Research Laboratory, Physical Sciences Division, Boulder, Colorado

(Manuscript received 17 January 2019, in final form 19 November 2019)

ABSTRACT

Precipitation variability over the Maritime Continent is predominantly explained by its diurnal cycle and large-scale disturbances such as the Madden–Julian oscillation (MJO) and convectively coupled equatorial waves (CCEWs). To advance our understanding of their interactions and physical processes, this study uses satellite data to examine changes in the diurnal cycle of rainfall associated with the MJO and CCEWs over the Maritime Continent. We find that diurnal cycle modulations associated with the passage of any type of large-scale disturbance are closely tied to changes in rain types and land–sea diurnal propagation of rainfall. When the amplitude of the diurnal cycle increases over the islands, the phase of the diurnal cycle is delayed by a few hours as clouds are more organized and rainfall from stratiform-anvil clouds increases. Enhanced amplitude of the diurnal cycle can alter the speed of land–sea diurnal propagation of rainfall, which then influences the timing of diurnal rainfall over coastal regions. These changes in the diurnal cycle occur asymmetrically across the island terrain associated with the MJO and equatorial Rossby waves, while such asymmetric modulations are not observed for other waves. Geographical and wave dependencies of the diurnal cycle are linked to differences in large-scale lower tropospheric wind, vertical motion, and moisture profile perturbations, which are in turn tied to differences in cloud population evolution. The results of this study highlight the importance of further improving our understanding of the sensitivity of cloud populations to varying large-scale phenomena.

1. Introduction

A large fraction of tropical rainfall and cloudiness variability is explained by the local diurnal cycle along with various modes of large-scale disturbances such as convectively coupled equatorial waves (CCEWs) and the Madden–Julian oscillation (MJO). Therefore, interactions between the diurnal cycle and the dominant modes of large-scale tropical variability are important for understanding and predicting rainfall in the tropics. However, current operational and general circulation models struggle to accurately simulate these phenomena (Kerns and Chen 2014; Li and Robertson 2015; Peatman et al. 2015; Dias et al. 2018; Janiga et al. 2018; Bengtsson et al. 2019). The interactions between the diurnal cycle and large-scale disturbances are further complicated over the Maritime Continent (MC) due to its unique combination of topography and land–sea contrasts. A number of studies have shown that the diurnal cycle of rainfall and cloudiness can vary with the MJO (e.g., Chen and Houze 1997; Sui et al. 1997; Tian et al. 2006; Rauniyar and Walsh 2011; Oh et al. 2012; Sakaeda et al. 2017, 2018), while only a few studies have examined the relationship between the diurnal cycle and CCEWs (Nguyen and Duvel 2008; Tulich and Kiladis 2012; Vincent et al. 2016). To fill this gap in knowledge, this study examines how the diurnal cycle of rainfall and cloudiness varies with CCEWs and the MJO over the MC. This study is motivated by the fact that the relationship between the diurnal cycle and large-scale atmospheric variability appears to depend on the mode of variability. An understanding of these dependencies could provide insights into the mechanisms of the

Corresponding author: Naoko Sakaeda, nsakaeda@ou.edu

DOI: 10.1175/JCLI-D-19-0043.1

diurnal cycle itself, and how that relates to large-scale equatorial wave perturbations.

The diurnal cycle is one of the fundamental modes of the atmosphere and is tied to the triggering and growth of cloud clusters, which tend to have a life cycle of a few hours to a few days—depending on their size (Chen and Houze 1997; Hennon et al. 2013). Kikuchi and Wang (2008) showed that the diurnal cycle explains over about 60%–70% of the total rainfall variability in the tropics, with higher percentage over land. The climatological diurnal cycle depends on the local topography, surface, and atmospheric characteristics. For this reason, the diurnal cycle of rain and cloudiness is different between land and open ocean, with primarily late afternoon peaks over land and early morning peaks over ocean (Yang and Slingo 2001; Nesbitt and Zipser 2003; Kikuchi and Wang 2008). Coastal areas often show offshore and onshore diurnal propagation of rainfall associated with land/sea breezes and induced gravity waves (e.g., Mapes et al. 2003b; Kikuchi and Wang 2008; Keenan and Carbone 2008; Biasutti et al. 2012; Hassim et al. 2016; Yamanaka et al. 2018).

Many studies have shown that the passage of the MJO modulates the amplitude and phase of the diurnal cycle of rainfall and cloudiness (e.g., Chen and Houze 1997; Sui et al. 1997; Rauniyar and Walsh 2011; Oh et al. 2012; Peatman et al. 2014; Sakaeda et al. 2017, 2018; Kerns and Chen 2018). The amplitude of the diurnal cycle of rainfall increases and the timing of the peak rainfall tends to be delayed by a few hours within the convectively enhanced envelopes of the MJO (Sakaeda et al. 2017). This delay is due to increased development of stratiform-anvil rainfall following the peak of deep convection (Sakaeda et al. 2017, 2018). Over most of the islands of the MC, the amplitude of the diurnal cycle is enhanced a few days prior to the passage of the center of the MJO enhanced envelopes (Oh et al. 2012; Peatman et al. 2014; Sakaeda et al. 2017). However, this relationship varies by event and geographically. On the east side of islands with high topography (i.e., Borneo, Sulawesi, and New Guinea), the amplitude of the diurnal cycle tends to peak a few days after the passage of the center of MJO enhanced envelope (Ichikawa and Yasunari 2006, 2008; Virts et al. 2013; Sakaeda et al. 2017). These observed changes in the diurnal cycle of rainfall are also suggested to play a role in the propagation of the MJO over the MC (Neale and Slingo 2003; Peatman et al. 2014, 2015; Majda and Yang 2016; Hagos et al. 2016) along with its convective initiation over Indian Ocean (Ruppert and Johnson 2015; Ruppert 2016).

Raupp and Silva Dias (2009) suggest that the diurnal cycle can also feed back onto other equatorial waves. Over the MC, Vincent et al. (2016) found evidence that the diurnal cycle of rainfall changes with convectively coupled Kelvin and equatorial Rossby (ER) waves in a manner similar to that of the MJO. Over equatorial Africa, Nguyen and Duvel (2008) showed that the passage of convectively coupled Kelvin waves enhances the development of diurnally triggered convective systems into larger organized systems, while the timing of the diurnal triggering is not significantly influenced. Chen and Houze (1997) documented a 2-day modulation of the diurnal cycle of cloud systems over the western Pacific basin, which enhances long-lived cloud system one day, followed by suppression of such development the next day. Chen and Houze (1997) suggested that this 2-day variability is associated with westward-propagating inertio-gravity (WIG) waves. Tulich and Kiladis (2012) also showed that the diurnal cycle of rainfall commonly propagates westward, which can trigger or be coupled to WIG waves. Some studies have also documented that the diurnal cycle over the islands of the MC can be phase-locked to convectively coupled Kelvin waves (Baranowski et al. 2016) and gravity waves (Ruppert and Zhang 2019).

Because diurnal land–sea breezes are considered to play a significant role in dynamically forcing the diurnal cycle of rainfall over the MC islands, several studies have suggested that the MJO influences the diurnal cycle over MC islands through the modulation of the lower-tropospheric wind, solar radiative heating, and moisture (Ichikawa and Yasunari 2006, 2008; Oh et al. 2012; Peatman et al. 2014; Vincent et al. 2016; Yanase et al. 2017; Wang and Sobel 2017; Yokoi et al. 2019; Lu et al. 2019). Therefore, one may expect the diurnal cycle to vary differently between CCEWs and the MJO if distinct perturbations of large-scale atmospheric profiles are a key factor determining the diurnal cycle characteristics. To test this hypothesis, this study uses TRMM/GPM and reanalysis data to investigate 1) how similarly or differently the characteristics of the MC diurnal cycle of rainfall vary with each CCEW and the MJO, and 2) which thermodynamic or dynamical features of the waves are associated with changes in the diurnal cycle.

2. Data and methodology

This study uses Tropical Rainfall Measuring Mission (TRMM) 3B42, TRMM Precipitation Radar (PR) from 3G68, Global Precipitation Measurement Mission (GPM) Dual-PR (DPR), and ERA-Interim (ERA-I) reanalysis data to examine the relationship between the CCEWs and the diurnal cycle of rainfall during November through March from 1998 to 2016. Both

CCEWs and the diurnal cycle are diagnosed using the same TRMM 3B42 rain rates in order to simplify the interpretation. If the diurnal cycle and CCEWs are diagnosed using different variables (e.g., brightness temperature for waves and rainfall for the diurnal cycle), the interpretation can be difficult because, for example, brightness temperature decreases with increased cirrus clouds, which do not produce significant amounts of rainfall.

a. TRMM and GPM data

TRMM 3B42 is 3-hourly, 0.25°-resolution global rainfall data between 50°N and 50°S generated using a combination of microwave and infrared estimates (Huffman et al. 2007). TRMM 3B42 is regridded to 0.5° horizontal resolution to match the resolution of TRMM 3G68, which includes gridded rainfall estimates from TRMM PR (2A25), which are only available along the path of TRMM satellite on an orbital period of about 90 min and 250-km swath width. This TRMM PR data do not provide continuous global coverage, but do provide three rain type classifications—convective, stratiform, and other (Iguchi et al. 2000). This study refers to all types of nonconvective rainfall as stratiform since nonstratiform and nonconvective rain types contribute only a few percent of total rainfall. TRMM was replaced by GPM in 2014, which includes a DPR instrument. We use the GPM DPR version 6 data to extend the TRMM 3G68 version 7 data. To generate continuous data before and after 2014, TRMM 3G68 was extended only using the rainfall estimates based on Ku-band of GPM DPR (KuPR), which have the same general design specifications as the TRMM PR. Rain estimates based on KuPR are gridded in the same manner as TRMM 3G68.

The comparison between gridded TRMM PR (3G68) and GPM DPR over the period of overlapping observations (1 April to 30 September 2014) showed general agreement (not shown). However, grid-averaged rainfall values between the two instruments sometimes do not match well because the orbital paths of the two instruments are different (Hou et al. 2014). The combined gridded PR/DPR data are available for about 5% of the 3-hourly data during the study period at each grid point, while availability is roughly evenly distributed among different times of day.

b. ERA-Interim reanalysis

The 6-hourly, 0.7° × 0.7° horizontal resolution ERA-I reanalysis from the European Centre for Medium-Range Weather Forecasts (ECMWF) is used to examine circulation and thermodynamic variables associated with the MJO and CCEWs. Radiosondes are typically launched twice daily over Indonesian islands, but the accuracy of the diurnal cycle of ERA-I variables is uncertain. Therefore, this study does not investigate the diurnal cycle of ERA-I variables, but uses them to examine the lower-frequency evolution of atmospheric profiles associated with the MJO and CCEWs.

c. CCEW identification

To identify CCEWs, TRMM 3B42 rainfall is filtered following the method of Wheeler and Kiladis (1999) using the same frequency–wavenumber bounding boxes as used in Dias et al. (2017). The left column of Fig. 1 shows the November–March variance of the filtered TRMM 3B42 rainfall—MJO, equatorial Rossby (ER), Kelvin, mixed Rossby–gravity (MRG), eastward inertio-gravity (EIG), and westward inertio-gravity (WIG) waves, which are referred to as wave modes throughout this manuscript. Since filtered anomalies include background noise, this methodology does not unambiguously identify each wave (Kiladis et al. 2016; Dias and Kiladis 2016). Therefore, we use empirical orthogonal function (EOF) analysis to extract the dominant modes of variability of filtered rainfall anomalies to verify that their structures are consistent with the theoretical structure of the waves from Matsuno (1966) over the MC.

The middle and right columns of Fig. 1 show TRMM 3B42 rainfall, 850-hPa ERA-I horizontal winds, and 850-hPa geopotential height anomalies associated with the first two leading EOFs of TRMM 3B42 rainfall that is filtered for each MJO/CCEW. The EOF analysis was applied to the filtered data over the MC region (10°N–12.5°S, 90°–165°E) to identify the structures of the dominant modes of variability over the region. Since the data are filtered for either eastward or westward propagation, the EOFs occur in pairs and together account for zonal propagation. The lower tropospheric circulation patterns associated with the two leading EOFs of filtered rainfall (and higher-order EOFs that are not shown) are consistent with the theoretical and observed structures (Wheeler et al. 2000; Kiladis et al. 2009), confirming that the dominant variability of the filtered TRMM 3B42 rainfall over the MC corresponds to CCEWs.

d. Estimation of the amplitude and phase of the diurnal cycle

Time series of the amplitude and phase of the diurnal cycle are obtained through harmonic analysis of TRMM 3B42 rain rate as done in Sakaeda et al. (2017). The diurnal harmonics are regressed onto the 3-hourly rain rate on each day, then the regression coefficients of the first diurnal harmonic are used to calculate the amplitude and phase of the diurnal cycle, which are hereafter referred to and represented as ''diurnal amplitude'' (δr)

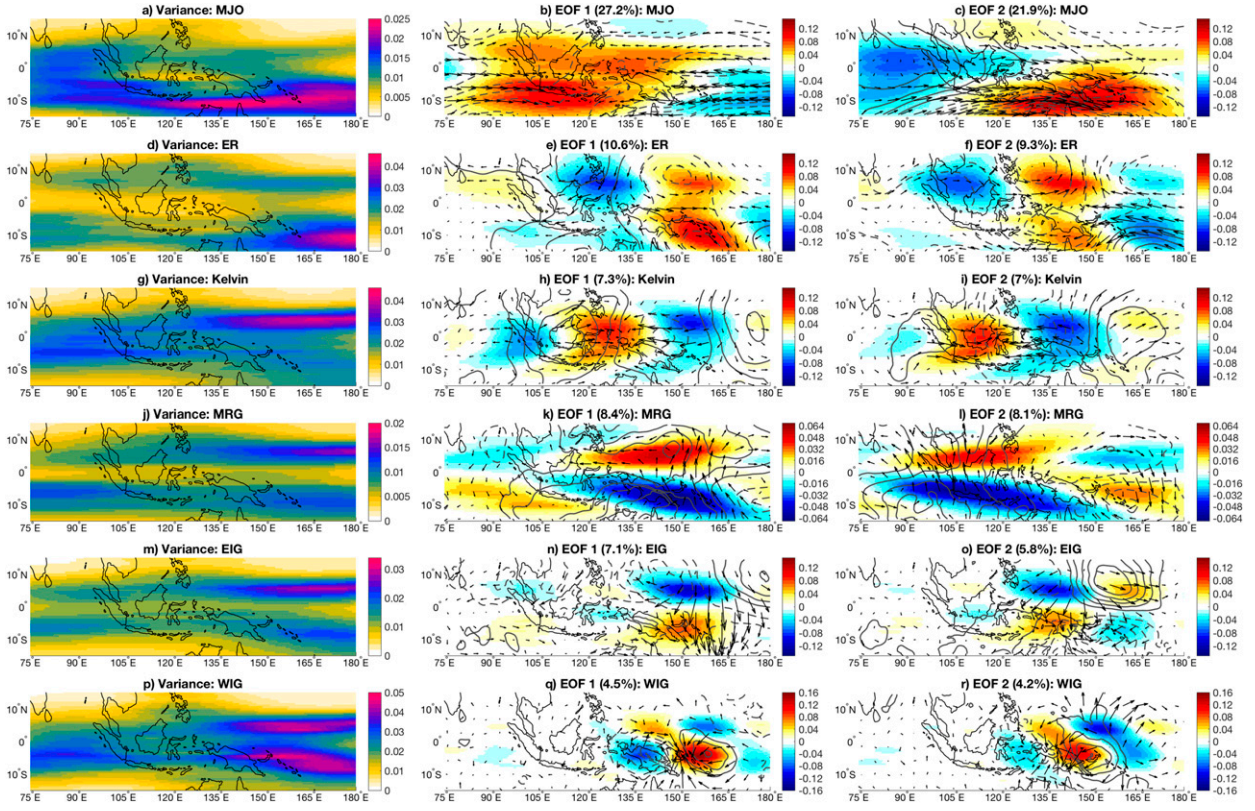

FIG. 1. (left) Variance of filtered TRMM 3B42 rain rate during November through March of the study period ($mm^2\,h^{-2}$). (middle),(right) Rainfall rate ($mm\,h^{-1}$; shaded), 850-hPa geopotential height (black contour), and 850-hPa horizontal wind (vector) anomalies associated with the first two leading EOFs of filtered TRMM 3B42 over the Maritime Continent (10°N–12.5°S, 90°–165°E). Each row shows the variance and leading EOF patterns of the TRMM 3B42 that is filtered for (a)–(c) MJO, (d)–(f) ER, (g)–(i) Kelvin, (j)–(l) MRG, (m)–(o) EIG, and (p)–(r) WIG waves. The solid contours indicate positive values and dashed contours indicate negative values. The geopotential height anomaly is contoured at 0.75 m for the MJO and ER, 0.25 m for the Kelvin, 0.2 m for the MRG, 0.1 m for the EIG, and 0.08 m for the WIG.

and "diurnal phase" (θr), respectively. The daily-mean rain rate is $\overline{r}$, where the overbar denotes average over a 24-h period throughout the manuscript. The diurnal amplitude (δr) is defined as the square root of the sum of the regression coefficients squared and the diurnal phase (θr) is calculated as the inverse tangent of the regression coefficients. The diurnal phase is then converted from UTC to local solar time (LST). The diurnal amplitude and phase are calculated using a running 24-h window that is centered at each 3-hourly time step (i.e., 0000 to 2100 UTC on day 1, 0300 UTC on day 1 to 0000 UTC on day 2, 0600 UTC on day 1 to 0300 UTC day 2, etc.). This is done to enable analysis of the relationship between the diurnal cycle and high-frequency waves such as EIG and WIG waves, which include periods of oscillation shorter than 2 days. We found that although some EIGs and WIGs over the MC appear to be phase-locked to the diurnal cycle, the majority of these events are not. While the harmonic analysis to estimate the diurnal amplitude and phase for each 24-h window may include noise, statistical analysis of their time series allows a detailed examination of how the diurnal amplitude and phase evolve separately within large-scale disturbances.

e. *Topography of MC islands*

Figure 2 shows the topography of the MC islands from NOAA/NESDIS ETOPO1 1 arc-min topography data (Amante and Eakins 2009) that is gridded to 0.5° × 0.5° resolution. Our discussion will focus on the five largest islands, New Guinea, Borneo, Sumatra, Sulawesi, and Java, that have mountain ranges with highest summits around 3–5 km.

3. Results

a. *Climatological diurnal cycle and rainfall properties*

Figure 3a shows the climatological daily-mean TRMM 3B42 rain rate and Fig. 3e shows mean PR rain rates over

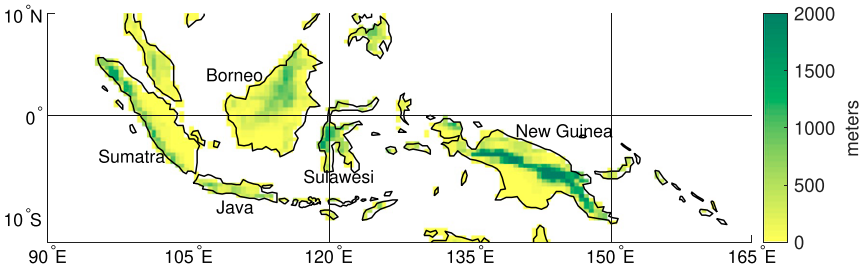

FIG. 2. Topography (m) of the Maritime Continents on 0.5° × 0.5° horizontal resolution.

the MC during November through March. Since the sampling of PR data is roughly evenly distributed over all hours of day, Fig. 3e represents the climatology of daily-mean PR rain rates. The spatial distribution of the mean rain rates from PR (Fig. 3e) generally agrees with the estimates from TRMM 3B42 (Fig. 3a), but the PR data are noisier because of their more limited sampling. PR estimates are lower than 3B42 rain rates due to overestimation of rain rates using microwave and infrared sensors that are used in TRMM 3B42 (Masunaga et al. 2002; Ikai and Nakamura 2003), which tend to occur within organized convective systems (Henderson et al. 2017).

Figure 3b shows strong diurnal amplitude over the MC islands and surrounding ocean. As shown by previous studies (Peatman et al. 2014; Sakaeda et al. 2017), diurnal amplitude (δr, Fig. 3b) tends to exceed the daily-mean rain rates ($\overline{r}$; Fig. 3a), especially over the islands (Fig. 3d). Where the diurnal cycle (i.e., 24-h harmonic) explains the majority of the intradiurnal variability, the ratio of diurnal amplitude to daily-mean values becomes close to one, which happens mostly over the ocean. When rainfall is more localized (i.e., has shorter duration), its projection onto the diurnal harmonics results in the ratio ($\delta r/\overline{r}$) being higher than one.

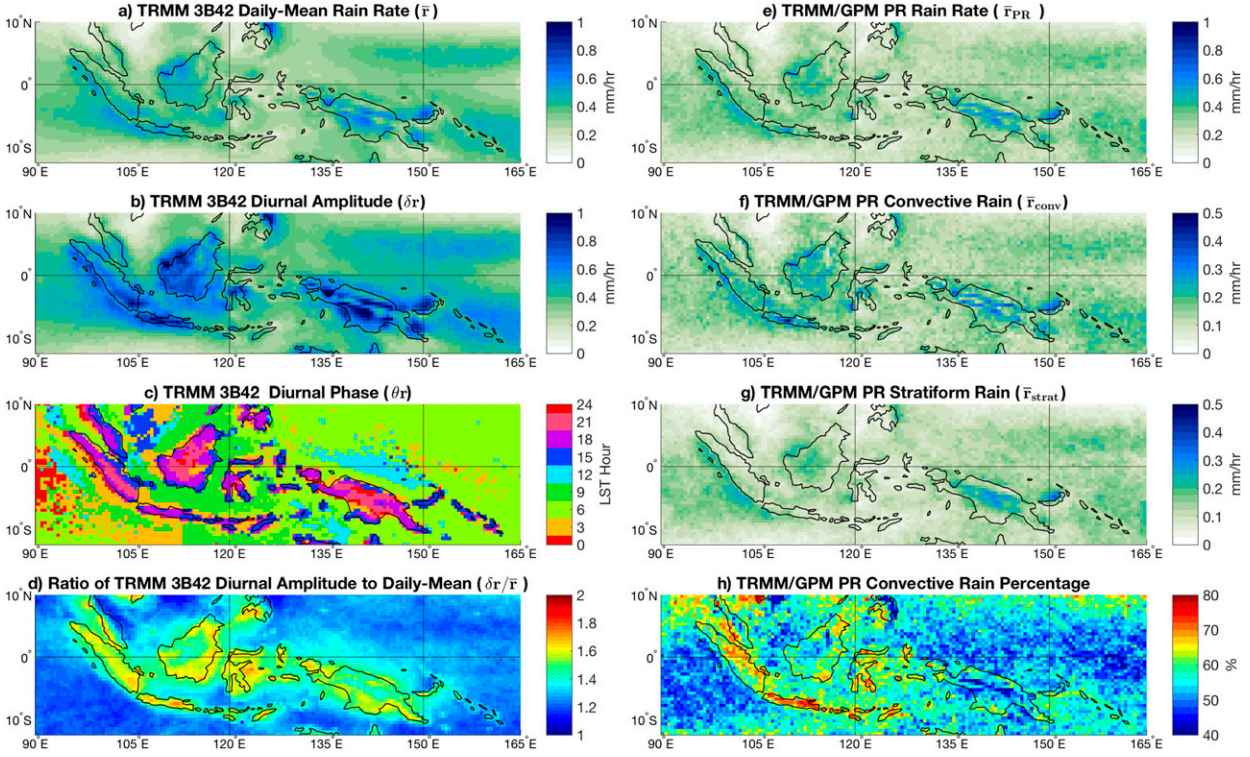

FIG. 3. Climatological rainfall properties over the Maritime Continent during the study period. Climatologically averaged (a) daily-mean ($\overline{r}$) and (b) diurnal amplitude of TRMM 3B42 rain rate (δr). (c) Climatological mode of the diurnal phase distribution of TRMM 3B42 rain rate (θr). (d) Ratio of the diurnal amplitude to daily mean TRMM 3B42 rain rate ($\delta r/\overline{r}$). (e) Mean total rain rate ($\overline{r}_{PR}$), (f) convective rain rate $\overline{r}_{conv}$, and (g) stratiform ($\overline{r}_{strat}$) rain rate of TRMM/GPM PR data. (h) Percentage of convective rain to total rain rate of TRMM/GPM data ($\overline{r}_{conv}/\overline{r}_{total}$).

Convective rain rates are generally higher over the islands where δr is high (Fig. 3f), while stratiform rain rates have less contrast in the amounts between land and ocean, except over New Guinea (Fig. 3g). Figure 3h shows the ratio of climatological mean PR convective to PR total rain rates. The contribution by convective rain tends to be greater over the islands where the $\delta r/\overline{r}$ ratio (Fig. 3d) is also large. The similar spatial distribution of these two quantities (Figs. 3d,h) suggests that the strong diurnal amplitude over the MC islands is primarily due to convective rather than stratiform rain. Over the ocean, drier areas also have a greater contribution from convective rain (e.g., outside the ITCZ and SPCZ bands), which suggests that isolated convective cells are more common than stratiform rain over those areas. These climatological maps of rainfall properties infer that the characteristics of the diurnal cycle relate directly to rainfall types and cloudiness.

The climatological diurnal phase (θr) is represented by the mode of its time series, which matches the climatological hour of peak diurnal rainfall shown by previous studies (e.g., Yang and Slingo 2001; Kikuchi and Wang 2008; Ling et al. 2019). In Fig. 3c, there are geographical discontinuities that appear in the climatological diurnal phase especially over the ocean (e.g., west of Sumatra, northeast of New Guinea island). These regions indicate the boundary between regular diurnal offshore propagation and where the diurnal cycle is relatively weak. When the diurnal cycle is weak and does not have a distinctly preferred phase, the identification of its mode becomes sensitive to the selection of bins and collected intervals of rainfall data. Over the islands, the diurnal phase indicates that rainfall propagates from the coast inland from late afternoon to midnight and propagates down the slope of topography to offshore from midnight into the early morning hours as shown by previous studies (e.g., Ichikawa and Yasunari 2006, 2008; Kikuchi and Wang 2008; Keenan and Carbone 2008; Biasutti et al. 2012). Over the surrounding ocean, rainfall peaks between early morning and noon.

b. Wave phase analysis

To diagnose the evolution of the diurnal cycle relative to the phase of the MJO and CCEWs, we composite data based on local phase of the MJO and CCEW convective envelopes. The local wave phase is defined by the time series of filtered TRMM 3B42 rain rates and its time tendency at each grid point as done in Riley et al. (2011) and Yasunaga and Mapes (2012b), which is referred to simply as "wave phase" (λ) in the rest of the manuscript. Figure 4 shows an example of the wave phase diagram defined by the wave-filtered rain rate (R_{wave}) and its time tendency (dR_{wave}/dt), both normalized by their standard deviation during the study period at each grid point. A wave phase (λ) of 0° is defined as the time of peak enhanced convective envelope and ±180° is defined as the center of the suppressed convective

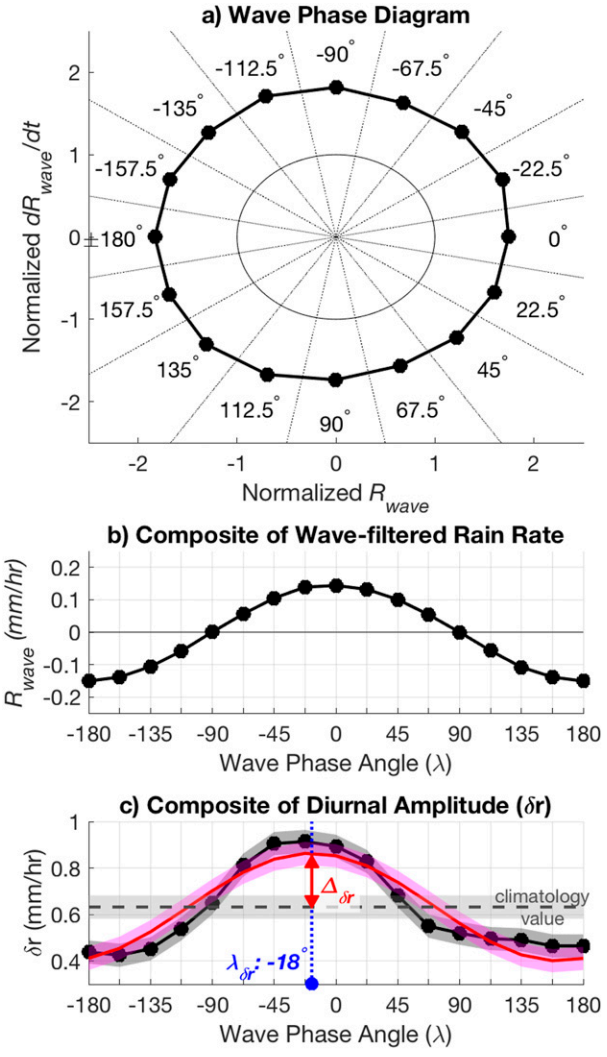

FIG. 4. (a) Local wave phase diagram using normalized wave-filtered rainfall and its tendency. Here 0° indicates the peak and ±180° indicates the minimum of the wave-filtered rainfall (i.e., enhanced and suppressed convective envelope, respectively). Negative degrees indicate that the enhanced convective envelope of a wave is amplifying and positive degrees indicate that it is decaying. (b) An example of a wave-filtered rain rate composited at each wave phase bin (λ). (c) An example of amplitude of the diurnal cycle (δr) that is composited at each wave phase bin (black line with dots). Red line shows a 360° harmonic that is projected onto the composite. The amount of change in δr with respect to the wave phase is defined as the amplitude of this harmonic ($\Delta_{\delta r}$) and the phase of the harmonic indicates when δr peaks with respect to wave phase ($\lambda_{\delta r}$). Gray dashed lines indicate climatological values. Magenta and gray shadings represent the confidence interval obtained from a bootstrap resampling.

envelope. Angles between ±90° correspond to the enhanced convective envelope where a negative angle means that it is amplifying or approaching and positive angle means decaying or propagating away. The amplitude of the wave is defined as the square root of the sum of squared values of the two time series. We analyze times when the amplitude of the wave is greater than 1. The wave phase is divided into 16 bins with 22.5° width (Fig. 4a) to derive statistics of the diurnal cycle characteristics. This technique allows us to examine the evolution of the diurnal cycle with the MJO and CCEW independent of differences in their period or propagation speed and direction (Figs. 4b,c).

Figure 4c demonstrates how a 360° harmonic analysis is applied to the wave phase composites to estimate how much the diurnal amplitude (δr) changes and when it peaks with respect to the wave phase, which are represented with symbols $\Delta_{\delta r}$ and $\lambda_{\delta r}$. Statistical significance of $\Delta_{\delta r}$ is tested by comparing its 95% confidence interval obtained by 1000-iteration bootstrap resampling to the confidence interval of noise, which is generated by randomly shuffling the order of wave phase (λ). Using this technique, the evolution of various quantities can be diagnosed with respect to the wave phase. Throughout the manuscript, Δ_X is used to represent the amount of change in a quantity X with respect to the wave phase and λ_X to represent the wave phase at which X peaks. This wave phase analysis technique is equivalent to the cross-spectral analysis method used by Sakaeda et al. (2017) but better eliminates background noise. Unlike the cross-spectral analysis, the wave phase technique does not require continuous time series, so the composites include only days with nonzero rain.

c. *Evolution of the diurnal cycle with the MJO and CCEWs*

1) DIURNAL AMPLITUDE OF RAINFALL RATE

A few studies have shown that the observed relationship between the diurnal amplitude (δr) and the MJO varies geographically within the MC (Oh et al. 2012; Peatman et al. 2014; Sakaeda et al. 2017). For the MJO, Figs. 5a and 5b show consistent results with Sakaeda et al. (2017), who used a cross-spectral analysis technique and OLR to represent the MJO instead of TRMM. Sakaeda et al. (2017) found that the relationship between δr and the MJO is weak over some islands, which is likely due to inclusion of noise in the MJO-filtered rain rate that is reduced using the wave phase analysis technique. This independent analysis confirms that δr tends to peak about 5–10 days (about −45° $\lambda_{\delta r}$) prior to the peak of the MJO enhanced convective envelope over the majority of the islands, especially on the western side of high topography. On the eastern side of the terrain, the relationship reverses and δr tends to peak about 5–10 days after the peak of the MJO enhanced convective envelope (i.e., positive $\lambda_{\delta r}$). This reversal of the relationship also appears over the ocean: $\lambda_{\delta r}$ tends to be positive over the ocean on the eastern side of islands while it tends to be slightly negative on the west side.

The wave phase relationship ($\lambda_{\delta r}$) of ER reverses its sign when compared to the MJO. For example, over the southwest side of New Guinea island, δr peaks when the MJO enhanced convective envelope is amplifying (i.e., negative $\lambda_{\delta r}$), but it peaks when the ER enhanced convective envelope is decaying (i.e., positive $\lambda_{\delta r}$). A similar reversal in $\lambda_{\delta r}$ between the MJO and ER appears throughout both land and oceanic regions of the MC. This reversed pattern of $\lambda_{\delta r}$ between the MJO and ER is expected if the diurnal amplitude increases on the leeward side of large-scale wind perturbations as suggested previously (Ichikawa and Yasunari 2006, 2008; Virts et al. 2013; Yanase et al. 2017). For example, the western side of most MC islands (Borneo, New Guinea, Sulawesi, and Sumatra) becomes the leeward side of the MJO wind anomaly when its convection is amplifying and becomes the leeward side when ER convection is decaying (Kiladis et al. 2009). This asymmetry in $\lambda_{\delta r}$ across the terrains also weakly appears with the MRG wave, but does not appear with other fast-propagating waves (Kelvin, EIG, and WIG). These fast waves uniformly slightly lag the peak δr (with a small negative $\lambda_{\delta r}$), especially over the MC islands, but with less of a phase lag between the timing of their peak enhanced convective envelopes and δr than the MJO and ER. The modulation of the diurnal amplitude by these fast waves cannot be explained through their lower tropospheric wind patterns in a consistent manner as the MJO and ER (as discussed in section 3d). In addition, slower waves (MJO and ER) tend to modulate the amplitude of the diurnal cycle more strongly over the ocean (larger $\Delta_{\delta r}$) than land, while this land–ocean contrast is less apparent for the other waves.

2) DIURNAL PROPAGATION OF RAINFALL RATE

The diurnal cycle of rainfall around the MC islands is strongly tied to the diurnal propagation of rainfall around the coastlines (Yang and Slingo 2001; Kikuchi and Wang 2008; Biasutti et al. 2012). To understand the mechanism by which the waves modulate the diurnal amplitude, it is important to first examine whether the changes in the diurnal amplitude occur through changes in the diurnal propagation of rainfall. The diurnal propagation characteristics are diagnosed with zonal and meridional propagation speeds of TRMM 3B42

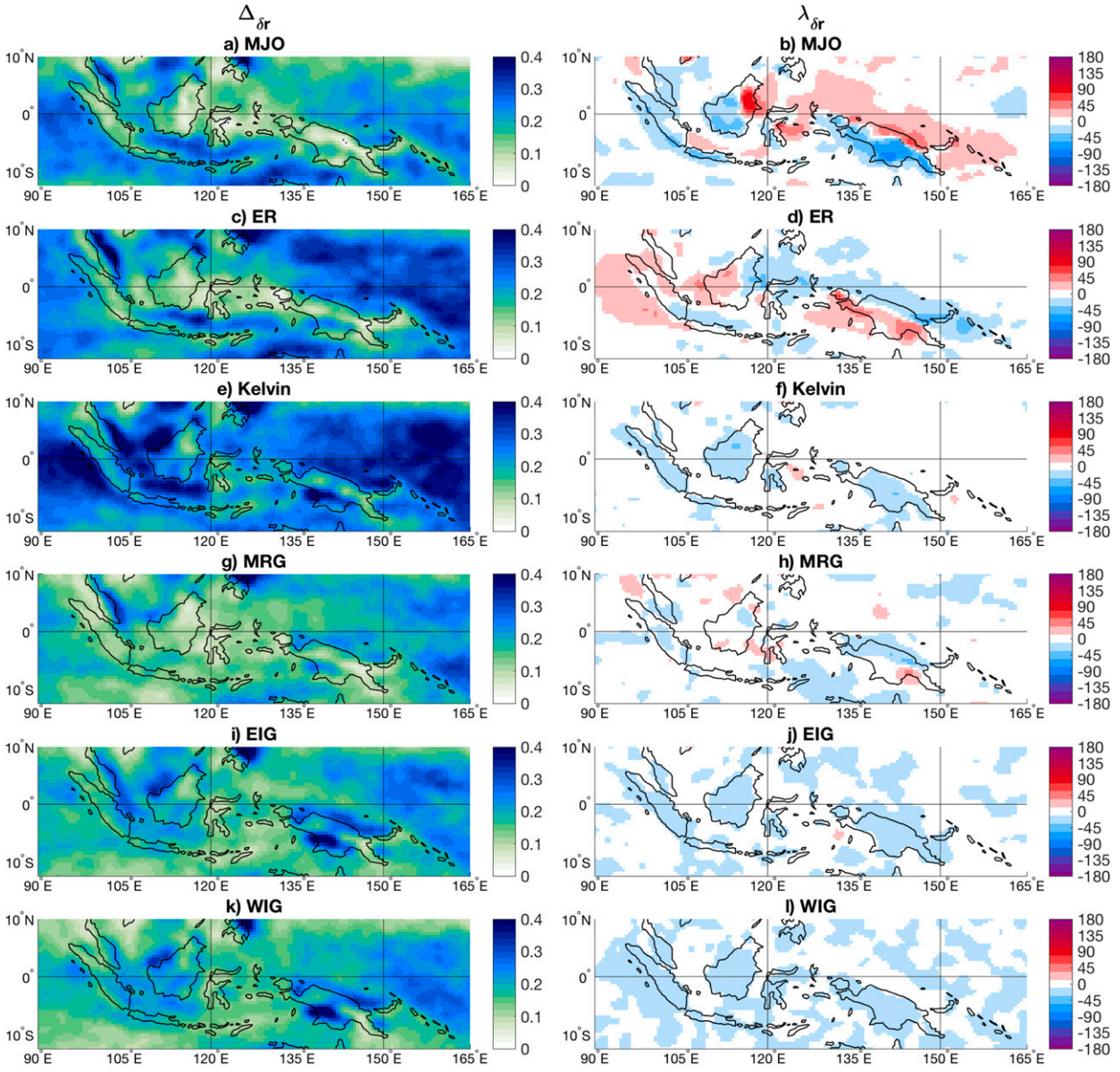

FIG. 5. (left) The amount of change in δr with respect to the wave phase ($\Delta_{\delta r}$; mm h^{-1}) and (right) wave phase at which δr peaks ($\lambda_{\delta r}$; degrees) at each grid point (see Fig. 4c). In the right column, negative $\lambda_{\delta r}$ indicates that the amplitude of the diurnal cycle leads the wave-filtered rainfall and positive $\lambda_{\delta r}$ indicates the opposite. The wave phase composite of δr is smoothed by applying 1–2–1 weighted average along the longitude and latitude directions three times and along the wave phase angle and hour of the day one time before calculating $\Delta_{\delta r}$ and $\lambda_{\delta r}$. The rows show $\Delta_{\delta r}$ and $\lambda_{\delta r}$ with (a),(b) the MJO, (c),(d) ER, (e),(f) Kelvin, (g),(h) MRG, (i),(j) EIG, and (k),(l) WIG-filtered rain rate.

rainfall that are estimated within a 2° box centered on each grid point. The diurnal propagation speeds are calculated using a running 24-h window in the same manner as for the diurnal amplitude and phase (see section 2d). Figures 6b and 6c demonstrate how the diurnal propagation speeds are estimated on a randomly selected date within a box labeled A in Fig. 6a. Within each 24-h window, the daily-mean rainfall rate is removed to generate the rainfall anomaly (r') that is averaged zonally (Fig. 6b) or meridionally (Fig. 6b) within the 2° box. Hours of maximum and minimum rainfall at each longitude and latitude are then used to calculate propagation speeds of positive and negative rainfall anomaly by fitting regression lines. The average of the propagation speeds of positive and negative rainfall anomalies is used to represent the diurnal

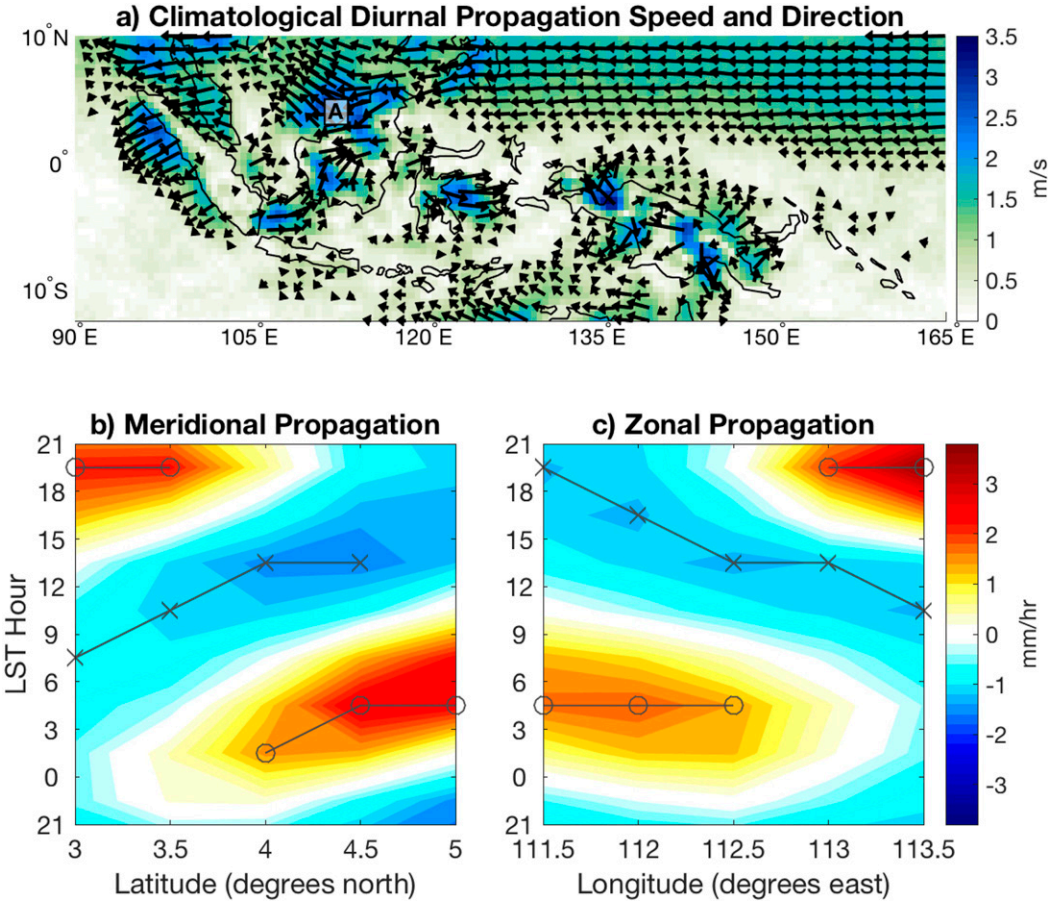

FIG. 6. (a) Climatological propagation speed ($m\,s^{-1}$; shaded) and direction (vectors) of rainfall. Propagation speed is calculated using the climatological zonal and meridional propagation speeds. Vectors are plotted where the total propagation speed exceeds $0.5\,m\,s^{-1}$. (b),(c) An example of rainfall anomaly from its daily-mean value averaged zonally and meridionally within box A shown in (a) on a randomly selected date. Gray lines with circles and crosses indicate time of maximum and minimum rainfall at each latitude and longitude, which are used to calculate the propagation speed of rainfall. See text for more details.

propagation of rainfall during each 24-h period and 2° box ($\mathbf{v}_r$). Given the selected 2° box, diurnal rainfall appears as stationary if rainfall propagates beyond 2° in less than 3 h (~$20\,m\,s^{-1}$). This method identifies the bulk diurnal propagation of rainfall that can be attributed to movement of individual precipitating systems, horizontal growth of precipitating systems, and initiation of new precipitating features (Sakurai et al. 2009; Hassim et al. 2016; Vincent et al. 2016; Yokoi et al. 2017), but the separate contributions from each of these factors cannot be distinguished.

The vectors in Fig. 6a show the average diurnal propagation speed and direction ($\mathbf{v}_r^{\text{climo}}$) during the study period. Shading shows the total diurnal propagation speed of the displayed vectors. The diagnosed diurnal propagation speeds are slower than some previously documented speeds (Ichikawa and Yasunari 2006, 2008; Yanase et al. 2017), which could be due to insufficient resolution to capture all propagating precipitating systems or the fact that previous studies often estimated diurnal propagation speeds from composite rainfall in contrast to our method of estimating diurnal propagation speeds each day and then taking its average. This diagnostic technique captures the well-documented land–sea propagation characteristics of the diurnal cycle around the MC islands (Kikuchi and Wang 2008; Biasutti et al. 2012). At latitudes 5°–10°N, Fig. 6a indicates that rainfall tends to propagate westward, likely due to the trade winds. Over this region, the diurnal phase is geographically uniform (Fig. 3c), which suggests that the propagation is not necessarily tied to the diurnal cycle. Therefore, our discussion focuses on the diurnal propagation of rainfall around the coastlines of MC islands.

To examine changes in the diurnal propagation of rainfall with the wave modes, zonal and meridional propagation speeds of diurnal rainfall are composited on the 16 wave phase bins (Fig. 4). The composited diurnal propagation speeds [$\mathbf{v}_r(\lambda)$] are then projected onto the climatological diurnal propagation speed ($\mathbf{v}_r^{\text{climo}}$; Fig. 6a) to obtain a scalar V, which represents either strengthening or weakening of diurnal rainfall propagation compared to its climatological direction:

$$V(\lambda) = \mathbf{v}_r(\lambda) \cdot \mathbf{v}_r^{\text{climo}} / |\mathbf{v}_r^{\text{climo}}|. \quad (1)$$

Figure 7 shows the anomaly of V from its climatological mean in shading and vectors showing the composited diurnal propagation speed and direction of rainfall [$\mathbf{v}_r(\lambda)$] at two selected wave phases. Positive and negative 90° wave phases are shown for the MJO and ER to demonstrate changes in the diurnal propagation when the diurnal amplitude increases on each side of the island terrain (Fig. 5). For the other waves, 0° and ±180° wave phases are shown, which are around when the diurnal amplitude maximizes and minimizes within those waves over the islands.

In general, diurnal propagation speed increases with the diurnal amplitude for all wave modes. During the amplifying phase of MJO convection ($\lambda = -90°$; Fig. 7a), offshore diurnal propagation of rainfall strengthens on the west side of terrain, while the diurnal propagation strengthens on the east side of terrain during the decaying phase of MJO convection ($\lambda = 90°$; Fig. 7b). In contrast to the MJO, offshore diurnal propagation of rainfall tends to strengthen on the east side of terrain during the amplifying phase of ER convection ($\lambda = -90°$; Fig. 7c). This result is consistent with previous studies (Ichikawa and Yasunari 2006, 2008; Virts et al. 2013) and indicates that offshore propagation of diurnal rainfall strengthens on the leeward sides of MJO and ER wind anomalies where the diurnal amplitude increases.

The relationship between the diurnal propagation speed and diurnal amplitude of rainfall appears consistently among the other waves (Kelvin, MRG, EIG, and WIG). Diurnal offshore propagation generally strengthens on both sides of terrain within enhanced convection (λ of 0°), and weakens within suppressed convection (λ of ±180°). This result suggests that these waves do not lead to changes in the preferred direction of diurnal propagation on either side of the terrain, indicating that they modulate the diurnal cycle through a different mechanism than in the MJO and ER. An increased convective rain over the islands by the fast-propagating waves appears to lead to faster propagation of diurnal rain, which is consistent with the expectation that the propagation speed of convectively generated gravity wave increases as the vertical wavelength of latent heating deepens (e.g., Mapes et al. 2003a; Beres et al. 2004; Hassim et al. 2016). Alternatively, the faster diurnal propagation may also be a result of the growth of more organized convective systems whose stratiform-anvil rainfall spread horizontally, or the initiation of new convective cells toward the offshore side (Sakurai et al. 2009; Yokoi et al. 2019).

3) Diurnal phase of rainfall rate

Since the diurnal propagation is strongly tied to the diurnal phase of rainfall around MC islands, variations in the diurnal propagation speed discussed in the previous section are expected to influence the diurnal phase. As discussed in Sakaeda et al. (2017), changes in the diurnal phase are difficult to detect through composites of 3-hourly rain rates, therefore, changes in the diurnal phase (θr) with waves are diagnosed using probability distribution functions (PDFs) of θr. We first explain our method to diagnose how much and when the PDF of diurnal phase shifts with respect to wave phase at each grid point, which is then used to interpret the relationship between diurnal propagation speed, diurnal amplitude, and diurnal phase. Figure 8a shows an example PDF of θr at each wave phase angle (λ) at one location. The PDF is then used as a weight to calculate mean diurnal phase, by first converting to hours from the mode of the PDFs at each wave phase bin [θ' in Eq. (2)].

$$\theta' = \theta - \theta_{\text{mode}}, \theta' = \{-12, +12\}, \quad (2)$$

where θ is a 3-hourly bin of the diurnal phase from 0000 to 2100 LST and θ' is converted to within ±12 h from the mode. For example, at $\lambda = 0°$ (Fig. 8b), the mode (θ_{mode}) is at 0900 LST, so then the 0600 LST bin (θ) becomes −3 h (θ') and the 1200 LST bin becomes +3 h. The weighted-mean hour from the mode (θ') is then calculated, weighted by the PDF of diurnal phase [$P(\theta)$] minus its minimum, which is added to the mode to find the weighted-mean diurnal phase [$\widehat{\theta r}$, Eq. (3)]:

$$\widehat{\theta r} = \theta_{\text{mode}} + \sum \theta' \times \{P(\theta) - \min[P(\theta)]\} / \sum \{P(\theta) - \min[P(\theta)]\}. \quad (3)$$

In Fig. 8b, the probability is higher at 0600 than 1200 LST, so the weighted-mean diurnal phase ($\widehat{\theta r}$) is slightly earlier than the mode (θ_{mode}). Figure 8c shows $\widehat{\theta r}$, calculated from the PDF shown in Fig. 8a, which captures the shifts in PDF of θr. A 360° harmonic is then projected to find the amount of change in diurnal phase ($\Delta_{\theta r}$ in hours) and the wave phase at which the diurnal phase delays the most with respect to the climatological

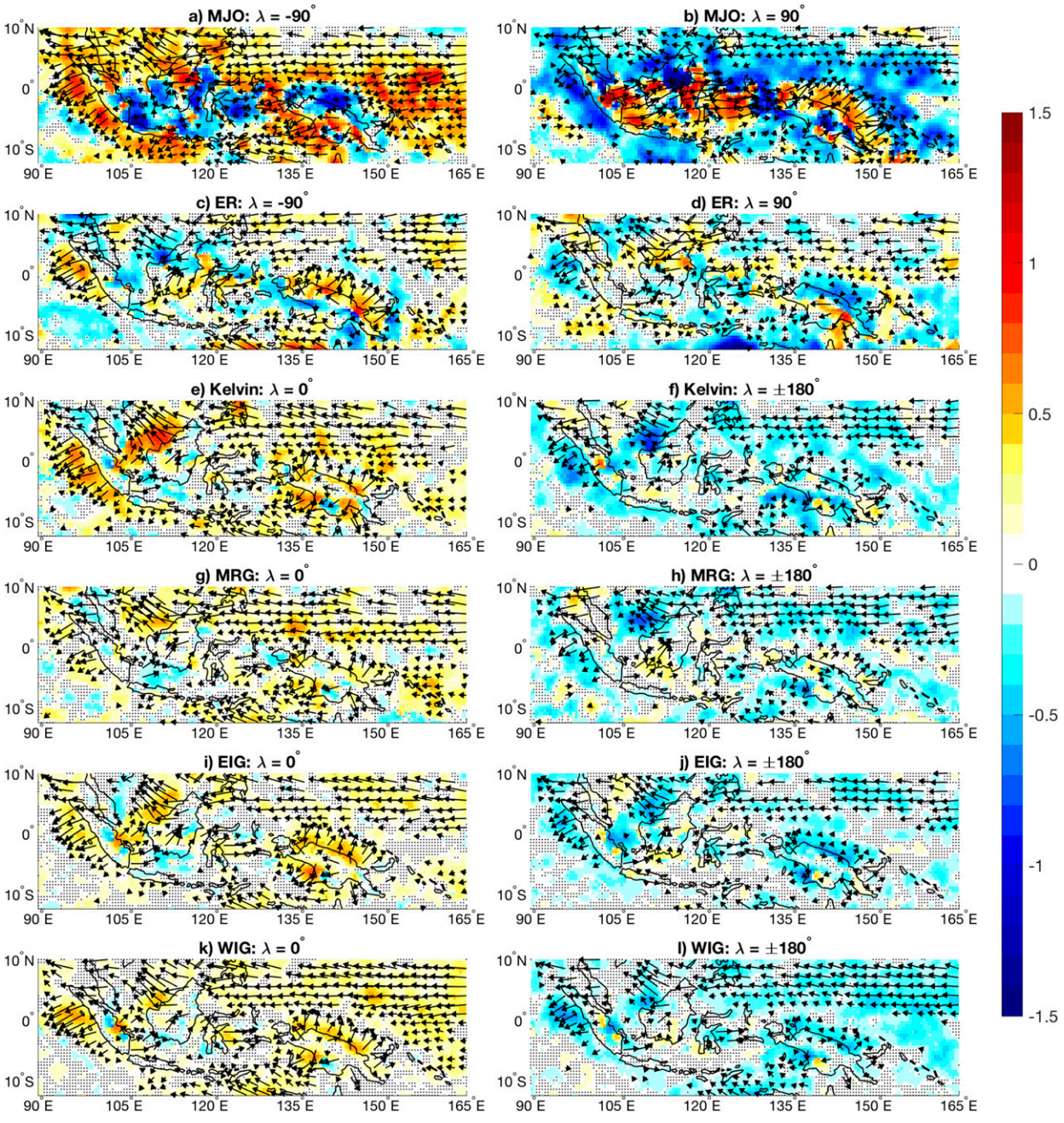

FIG. 7. Propagation speed and direction of diurnal rainfall (vectors) and its projection onto climatological propagation of rainfall [V in Eq. (1); shaded] for two opposing wave phases of each wave. Areas where V is not statistically significantly different from zero are indicated with black dots. Vectors are plotted where the propagation speed exceeds 0.5 m s^{-1} and V is statistically significant. (a),(b) −90° and 90° wave phase of the MJO, (c),(d) −90° and 90° of ER, (e),(f) 0° and ±180° of Kelvin. (g),(h);(i),(j);(k),(l) Same angles as in (e),(f), but for MRG, EIG, and WIG, respectively. The wave phase composites of V and $\mathbf{v}_r(\lambda)$ are smoothed by applying 1–2–1 weighted average along the longitude and latitude directions three times and along the wave phase angle and hour of the day one time.

diurnal phase ($\lambda_{\theta r}$). As shown in the example in Fig. 8, θr is modulated by less than ±1 h over most of the islands by all wave modes ($\Delta_{\theta r} \leq 1$). Statistical significance of $\Delta_{\theta r}$ is tested in the same manner as for $\Delta_{\delta r}$. Figure 9 shows $\lambda_{\theta r}$ calculated at each grid point where $\Delta_{\theta r}$ is statistically significantly different from zero at the 95% confidence level.

Although Fig. 9 appears noisy, some consistency between $\lambda_{\delta r}$ (right column of Fig. 5) and $\lambda_{\theta r}$ can be found over the larger islands. For example, over New Guinea

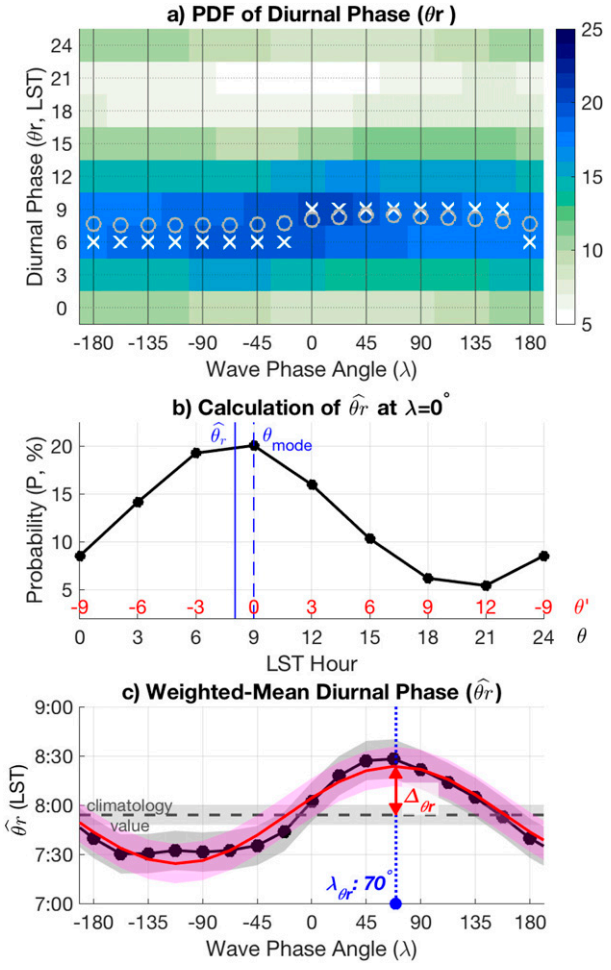

FIG. 8. (a) An example of probability distribution functions (PDFs; in %) of the phase of the diurnal cycle (θr) in LST hours within each local wave phase bin (Fig. 4). The white crosses are the modes and gray circles are the weighted-mean phase of the diurnal cycle ($\widehat{\theta r}$), as calculated using Eq. (3). (b) Example of how $\widehat{\theta r}$ is calculated at $\lambda = 0°$ using the PDF of diurnal phase (black line). The mode of the PDF (θ_{mode}) is shown by the vertical dashed blue line, which is 0900 LST in this case. The hours from the mode of the PDF [θ'; Eq. (2)] are shown in red along the horizontal axis. Note that $\widehat{\theta r}$ is calculated using Eq. (3) as the weighted mean of θ' by the PDF added to θ_{mode}. (c) As in Fig. 4c, but showing an example of weighted-mean phase of the diurnal cycle ($\widehat{\theta r}$, black line with dots), projected one cycle harmonics (red), and climatological weighted-mean phase of the diurnal cycle (gray dashed). The amount of change in $\widehat{\theta r}$ with respect to the wave phase is defined as the amplitude of the projected harmonic ($\Delta_{\theta r}$) and the phase of the harmonic indicates when $\widehat{\theta r}$ delays the most with respect to wave phase ($\lambda_{\theta r}$).

and Borneo, the diurnal phase delays on the west side of the topography when MJO enhanced convection is amplifying (negative $\lambda_{\theta r}$), while it delays on the east side when MJO convection is decaying (positive $\lambda_{\theta r}$, Fig. 9a), consistent with the signs of $\lambda_{\delta r}$ in Fig. 5b. This pattern is reversed for the ER waves as was seen with the diurnal amplitude: the diurnal phase delays on the west side when ER enhanced convection is decaying (positive $\lambda_{\theta r}$ on the west side; Fig. 9b). These results indicate that, over land, increased diurnal amplitude is associated with an increase in the organization of clouds with longer lifetime and greater horizontal extent, leading to the delayed diurnal phase (Sakaeda et al. 2017, 2018). However, the patterns of $\lambda_{\theta r}$ over ocean associated with the MJO, ER, and MRG are noisy and highly dependent on geographical location. This noisiness partially results from the opposite signs of $\lambda_{\theta r}$ that appear on ocean and land sides of coastlines. For example, over the east side of Borneo and northeast side of New Guinea, $\lambda_{\theta r}$ of the MJO is positive on land but becomes negative on the ocean side of coastal area. This contrast in $\lambda_{\theta r}$ between the land and sea sides of coastline can be explained by the changes in the offshore propagation speed of diurnal rainfall discussed in the previous section. On the landward side of coastal areas, when convection and diurnal amplitude strengthen, enhanced organized convection delays the diurnal phase, while it propagates faster offshore. This faster offshore propagation of rainfall causes the coastal oceanic rainfall to occur at an earlier time of day. Therefore, when the diurnal phase is delayed over land, it becomes earlier over coastal ocean, and when it becomes earlier over land, it is delayed over ocean due to slower offshore propagation. Over the open ocean away from the MC islands, where the land–sea propagation of rainfall does not strongly influence the diurnal cycle, $\lambda_{\theta r}$ tends to become closer to 0° (i.e., around the center of waves' enhanced convective envelopes). This suggests that, where the land–sea propagation does not drive the diurnal cycle of rainfall, the diurnal phase is delayed as clouds become more organized and stratiform rain increases (Sakaeda et al. 2017, 2018).

Kelvin, EIG, and WIG waves also show sharp contrast in $\lambda_{\theta r}$ over land and ocean but are more uniform within land or ocean points. This land–sea contrast can also be explained through the changes in the offshore propagation speed of diurnal rainfall. Over the islands, the diurnal phase is generally delayed within or slightly ahead of enhanced convective envelopes, which is when the diurnal amplitude peaks (Figs. 5f,j,l). As shown in sections 3c(1) and 3c(2), when the diurnal amplitude strengthens within these waves, rainfall propagates offshore at a faster speed on both sides of terrain. The faster offshore propagation of rainfall leads the surrounding ocean rainfall to occur earlier, while the diurnal phase over ocean is delayed when the diurnal amplitude weakens over islands and propagates offshore more slowly. The geographical pattern of $\lambda_{\theta r}$ appears more uniform over ocean for Kelvin, EIG, and WIG waves because these modes modulate the diurnal

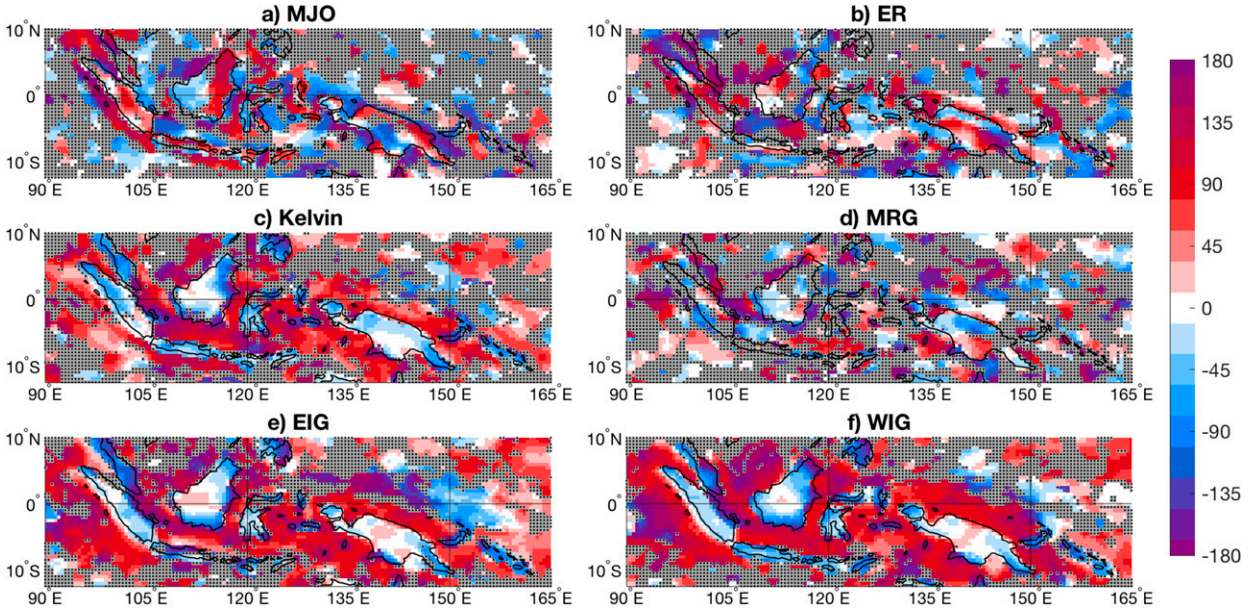

FIG. 9. Wave phase at which the weighted-mean diurnal phase is most delayed ($\lambda_{\theta r}$), calculated as shown in Fig. 8 at each grid point, for (a) MJO, (b) ER, (c) Kelvin, (d) MRG, (e) EIG, and (f) WIG. The PDFs are smoothed by applying a 1–2–1 weighted average along the longitude and latitude directions three times and along the wave phase angle and hour of the day one time. The gray shading with black dots indicates points where $\Delta_{\theta r}$ (defined in Fig. 8b) is not statistically significantly different from zero at the 95% confidence level.

propagation of rainfall simultaneously over both sides of island topography (Fig. 7). These results show that, compared to the open ocean (e.g., Sakaeda et al. 2018), the modulation of the diurnal phase is complicated by the existence of the diurnal propagation of rainfall around the coastlines, whose evolution also depends on the wave mode.

4) MODULATIONS OF RAINFALL PROPERTIES

This section further examines the evolution of diurnal cycle by using PR convective and stratiform rain rates, in order to understand their contribution to changes in the diurnal amplitude, phase, and propagation. Each panel of Fig. 10 shows daily-mean values of convective and stratiform rain (red and blue lines on top) and their anomalies from daily mean values (shadings and contours) at each wave phase bin averaged over all MC land and ocean points separately. Each 0.5° grid box is classified as land if the fraction of land points from ETOPO1 is greater than 0.1; otherwise, it is classified as ocean. Since the evolution of the diurnal cycle with the MJO and ER is more geographically dependent, the points where $\lambda_{\delta r}$ is negative in Fig. 5b are only included for the MJO (69% of points over land and 46% over ocean) and only positive $\lambda_{\delta r}$ points in Fig. 5d are included for the ER (52% of points over land and 38% over ocean). These geographical averages demonstrate the general evolution of rain types with the diurnal cycle while neglecting details of the geographical variability shown in Figs. 5 and 9. The diurnal evolution of cloud populations and rain types can vary significantly by island (e.g., Mori et al. 2004; Ichikawa and Yasunari 2006, 2008; Qian 2008; Tabata et al. 2011; Fujita et al. 2011; Yanase et al. 2017; Yokoi et al. 2019), and such island-by-island details are beyond the scope of this study. Over land, daily convective rain amount is greater than stratiform rain, while their amounts are more comparable over ocean (Houze et al. 2015). For the MJO over land and Kelvin, EIG, and WIG waves, the peak of convective rain leads the peak of stratiform rain, while the MJO over the ocean and ER and MRG waves have convective and stratiform rain increasing simultaneously. These results are consistent with the evolution of cloud populations associated with the passages of the MJO and CCEWs by previous studies (e.g., Takayabu and Murakami 1991; Takayabu 1994; Benedict and Randall 2007; Kiladis et al. 2009; Yasunaga and Mapes 2012a,b; Vincent and Lane 2018).

The diurnal amplitude generally peaks when total rainfall peaks for all wave modes. Because convective rain dominates over land and it leads stratiform rain [also shown in Vincent and Lane (2018)], the diurnal amplitude peaks at an earlier wave phase than over ocean, except for ER and MRG waves. Daily convective and stratiform rain evolve more simultaneously for ER and MRG waves, which still appear over most geographical points (not shown). For all wave modes

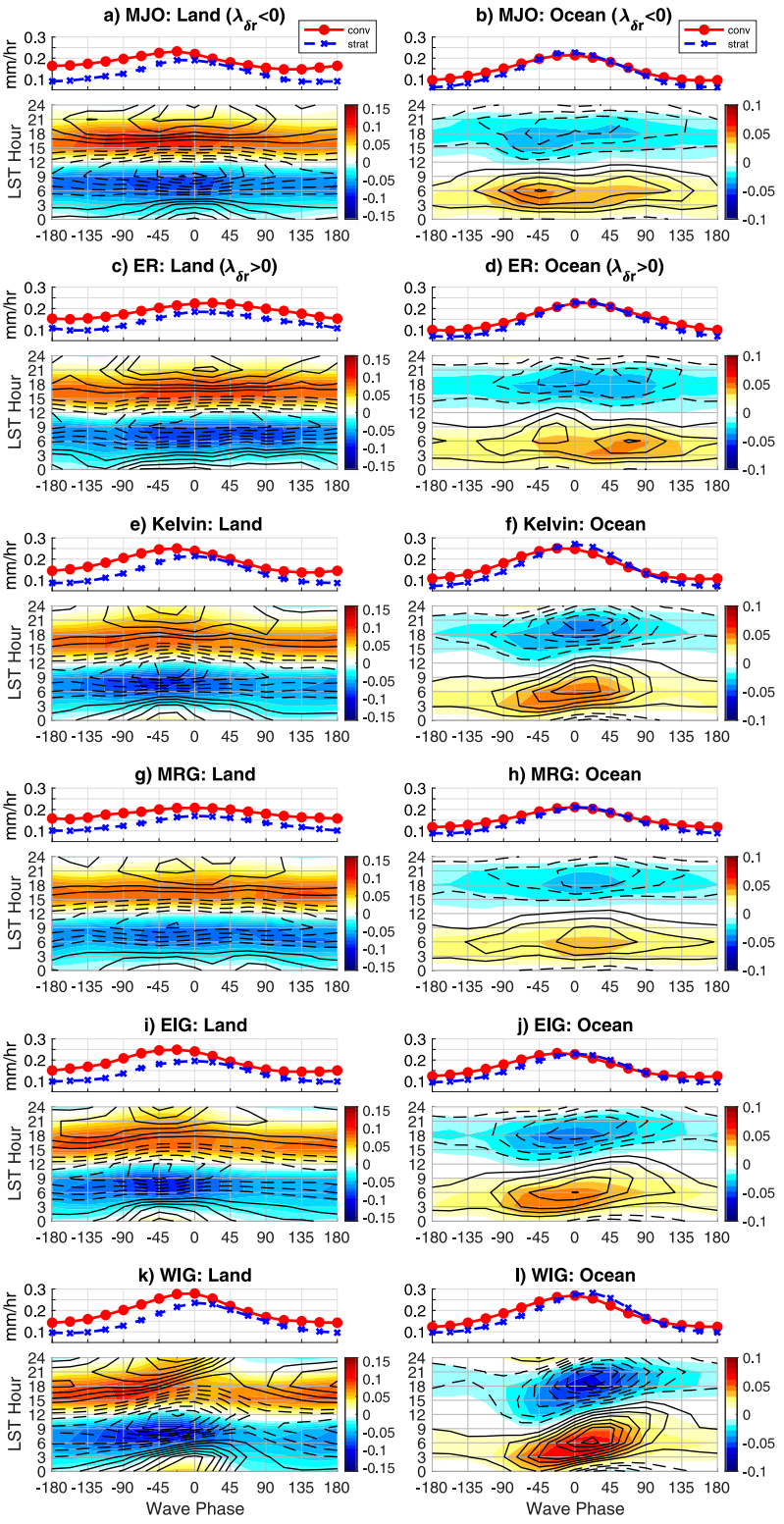

FIG. 10. Composites of PR convective and stratiform rain rates based on the wave phase bins over (left) land and (right) ocean points within the Maritime Continent (10°N–12.5°S, 90°–165°E). (a),(b) Composites for the MJO only include points where $\lambda_{\delta r}$ is negative in Fig. 4 and (c),(d) positive $\lambda_{\delta r}$ points for ER. Red and blue lines at the

and wave phases, the diurnal peak of convective rain (around 1500–1800 LST over land and 0300–0600 LST over ocean) is followed by the peak of stratiform rain (around 2100–2400 LST over land and 0600–0900 LST over ocean). The diurnal phase of either rain type does not change significantly with the passage of the MJO, ER, and MRG waves. Therefore, when the geographical variability around the coastlines is excluded, the delayed diurnal phase corresponds to when daily stratiform rain fraction increases during the passage of the MJO, which is also true for ER and MRG.

During the passage of Kelvin, EIG, and WIG waves, the evolution of the diurnal cycle shows clear differences over land and ocean, despite the similarity in the evolution of daily convective and stratiform rain. Over land, Figs. 5 and 9 showed that the diurnal amplitude strengthens and diurnal phase is delayed slightly before their enhanced convection peaks (−45°–0°λ), which also appears with the PR convective and stratiform rain (Figs. 10e,i,k). The amount of stratiform rain increases as the diurnal phase is delayed, indicating the increased development of stratiform cloud systems that are longer-lived or larger in horizontal space. Over the ocean, the diurnal amplitude of PR convective and stratiform rain strengthens around 0° λ in Kelvin, EIG, and WIG waves, consistent with Fig. 5. However, in contrast to land, Figs. 10f, 10j, and 10l show that the diurnal phase continues to be delayed within decaying convective envelopes of the waves over ocean (45°–90°λ), due to the slowing down of offshore propagation of rainfall from the islands. These results confirm the finding with TRMM 3B42 in the previous sections that oceanic rainfall around the islands occur at an earlier time of day when the diurnal cycle strengthens inland and propagates offshore at a faster speed. These results show that the changes in the diurnal phase around MC islands are due to both changes in rain types and diurnal propagation of rainfall.

d. Modulation of large-scale atmospheric perturbations

1) LOWER TROPOSPHERIC ZONAL WIND

Previous studies suggest that the diurnal propagation of rainfall around the large islands of the MC (e.g., Java, Borneo, and New Guinea) depends on the direction of lower tropospheric large-scale zonal wind and vertical wind shear (Mori et al. 2004; Sakurai et al. 2005; Ichikawa and Yasunari 2006, 2008; Sakurai et al. 2009; Virts et al. 2013; Yanase et al. 2017; Yokoi et al. 2019). Using a cloud-permitting model, Wang and Sobel (2017) also found that the diurnal cycle of rainfall over islands is enhanced when large-scale wind is weak, while a strong large-scale wind leads to more asymmetry in the amount of rainfall across the terrain. The results from the previous sections suggest that the contrasting modulation of the diurnal cycle by the waves may be partially explained by their varying circulation patterns. To investigate the role of lower tropospheric wind, Fig. 11 shows daily 850-hPa horizontal wind direction and speed anomalies at the two wave phases as shown in Fig. 7 that correspond to when the diurnal amplitude and propagation maximizes and minimizes within each wave mode. Wind anomalies are calculated by removing its annual mean and first three seasonal harmonics.

In agreement with previous studies (e.g., Ichikawa and Yasunari 2006, 2008), Figs. 11a and 11b show that the diurnal amplitude and offshore propagation are enhanced on the leeward side of 850-hPa flow associated with the MJO (Figs. 5a and 7a,b). Although the magnitude of wind anomalies is weaker, ERs induce flow that is directed opposite from the MJO in some areas at the same wave phase (e.g., over Borneo and northeastern New Guinea), consistent with their contrasting effects on diurnal amplitude and propagation over those areas (Figs. 7c,d). The 850-hPa anomalous flow associated with the MJO and ERs generally aligns with the direction of anomalous vertical shear of lower tropospheric horizontal wind (not shown), suggesting that these waves influence the diurnal propagation direction of rainfall through horizontal advection of clouds and initiation of new convective cells in the direction of the shear (LeMone et al. 1998; Sakurai et al. 2009; Yokoi et al. 2019).

However, no consistent patterns of 850-hPa winds are found among the other wave modes. For example, the diurnal amplitude over the northeastern side of New Guinea peaks at $\lambda = 0°$ for EIGs and WIGs associated with their northerly to northeasterly winds, whereas it

←

top of each panel show daily-mean convective and stratiform rain rates, respectively. Shading and contours show composites of 3-hourly convective and stratiform rain rate anomalies (mm h^{-1}) from daily-mean value at each wave phase angle. Contours are plotted at 0.01 mm h^{-1} interval and solid (dashed) lines indicate positive (negative) values. Data are smoothed by applying a 1–2–1 weighted average along the wave phase angle and hour of the day.

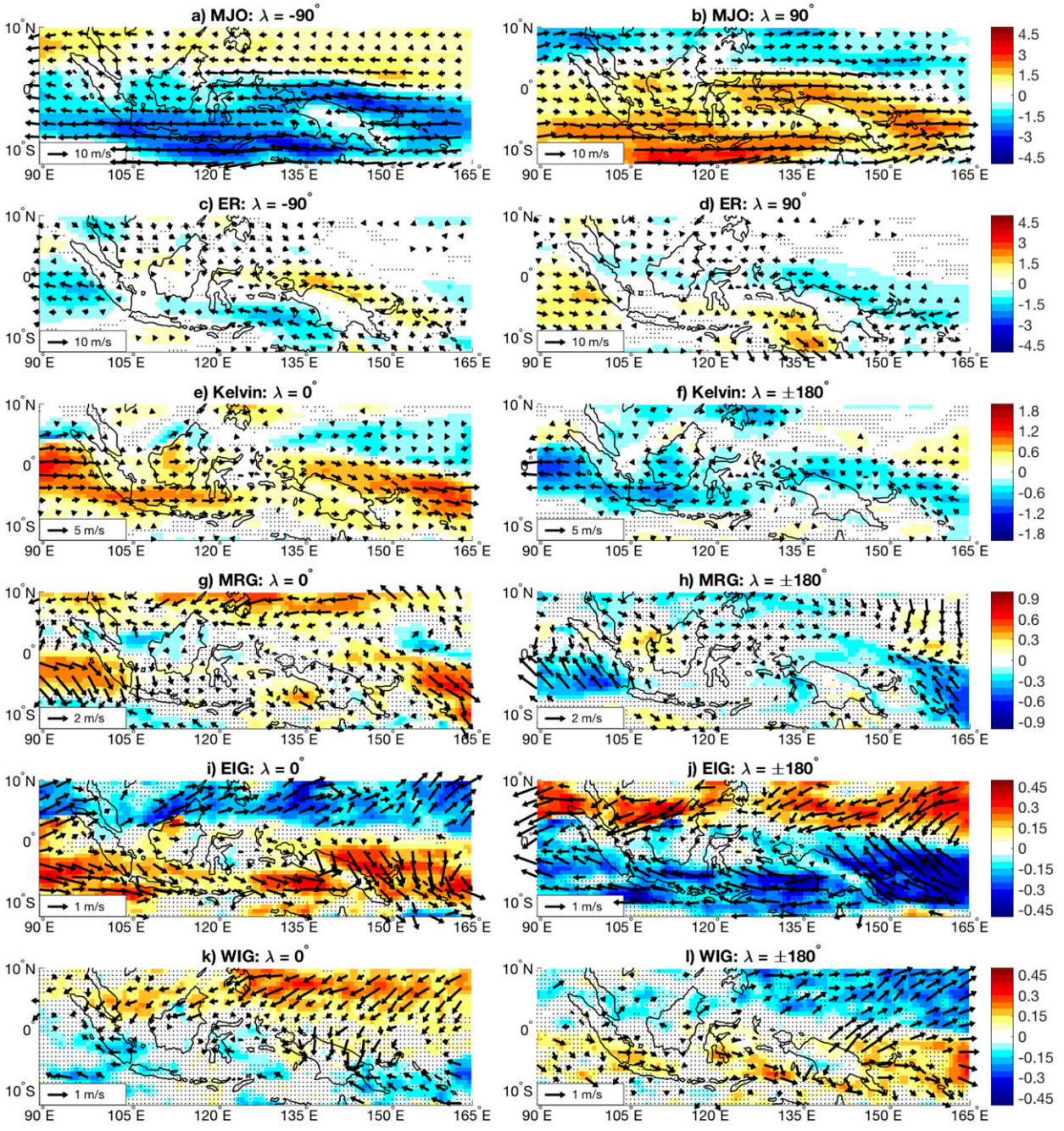

FIG. 11. Composite of 850-hPa horizontal wind anomaly (vector) and speed anomaly from climatology ($m\,s^{-1}$; shaded) for the two opposing wave phases of each wave shown in Fig. 7. Black dots indicate points where the wind speed anomaly is not statistically significantly different from zero at the 95% confidence level. Wind anomaly vectors are plotted where the wind speed anomaly is statistically significant. The wave phase composites are smoothed by applying 1–2–1 weighted average along the longitude and latitude directions three times and along the wave phase angle and hour of the day one time.

peaks at $\lambda = 0°$ for Kelvin within northwesterly winds. The directions of the anomalous 850-hPa flow (or lower tropospheric vertical shear; not shown) are not aligned with the preferred direction of diurnal rainfall propagation in Fig. 7. However, the magnitude of wind anomalies associated with the faster-propagating waves (Kelvin, EIG, and WIGs) is about one-tenth of that associated with the MJO and ER. Therefore, winds associated with the faster-propagating waves may not be strong enough to mechanically modulate rainfall around

the islands (Wang and Sobel 2017), suggesting that those waves modulate the diurnal cycle through different mechanisms. This result demonstrates that the lower tropospheric wind alone does not control the strength or propagation of the diurnal cycle for all wave modes over the MC region.

2) HUMIDITY PROFILES

Tropical rainfall is also known to increase with the amount of column humidity (e.g., Bretherton et al. 2004; Holloway and Neelin 2009; Ahmed and Schumacher 2015). Moisture generally builds from the lower troposphere ahead of the MJO/CCEW convective envelope, and then deepens as its convective envelope passes. However, contrasts in the vertical structure of the MJO and CCEWs have been documented (Yang et al. 2007; Kiladis et al. 2009; Inoue et al. 2019, manuscript submitted to *J. Atmos. Sci.*), which may relate to the differences in their modulation of the diurnal cycle over the MC.

Figure 12 shows the wave phase composite of vertical profiles of daily specific humidity (q, shaded) and vertical motion (pressure velocity ω, in black contours) anomalies for all land and oceanic points within the MC region (note the difference in the shaded color scales for each wave). Passage of an MJO convective envelope is associated with a slightly greater vertical tilt of moisture over land than ocean. As shown in Kiladis et al. (2009), the moisture profile of the ER is more vertically stacked over the ocean and negatively tilted with altitude over land. The amplitude of specific humidity anomalies is greatest over a deep tropospheric layer (400–800 hPa) with the MJO, ER, and MRG, but it is greatest in the lower troposphere (below 600 hPa) with the Kelvin, EIG, and WIG. The humidity anomaly is also greater over the ocean than land with the MJO, ER, and MRG. The other faster propagating waves (Kelvin, MRG, EIG, and WIG) show more accentuated vertical tilts in humidity and a stronger humidity anomaly is confined within the lower troposphere below 600 hPa. Similar to humidity, the vertical profiles of vertical motion show consistent differences among the waves (Inoue et al. 2019, manuscript submitted to *J. Atmos. Sci.*) Greater vertical tilt in the vertical motion appears with Kelvin, EIG, and WIG over both land and ocean, and with the MJO over land. The transitions from bottom-heavy to top-heavy profiles of the vertical motion within the Kelvin, EIG, and WIG waves coincide with the transition from convective to stratiform rain (Fig. 10). In contrast, the MJO, ER, and MRG waves are associated with less vertical tilt and top-heavy vertical profiles throughout their cycles, which coincide with a more simultaneous increase in convective and stratiform rain. The moisture and vertical motion tend to evolve simultaneously for the MJO and ER, but the midtropospheric vertical motion tends to lead the moisture for other faster-propagating waves, suggesting that dynamically forced vertical motion leads to column moistening [as shown in Inoue and Back (2015)].

To examine how specific humidity and vertical motion relate to the modulation of the diurnal cycle of rainfall, daily column-integrated specific humidity and midtropospheric pressure velocity are composited on the wave phase (Fig. 4). The column-integrated specific humidity $[\overline{q}]$ represents the mass-weighted vertical integral from 1000 to 200 hPa and the midtropospheric pressure velocity ($\overline{\omega}_{\text{mid}}$) is vertically integrated from 800 to 400 hPa. As shown in Figs. 4c and 8c, a 360° harmonic is projected to find the wave phase at which the column specific humidity peaks ($\lambda_{[\overline{q}]}$) and midtropospheric pressure velocity minimizes (i.e., peak ascent, $\lambda_{\overline{\omega}_{\text{mid}}}$) at each grid point. Figure 13 shows $\lambda_{[\overline{q}]}$ and $\lambda_{\overline{\omega}_{\text{mid}}}$ plotted against $\lambda_{\delta r}$ from Fig. 5. If these variables evolve simultaneously with diurnal amplitude, the plotted points in Fig. 13 should be along the one-to-one (black) line.

For the MJO, ER, Kelvin, and MRG waves, $\lambda_{[\overline{q}]}$ aligns with $\lambda_{\delta r}$, indicating that the diurnal cycle generally strengthens as column moisture increases. However, Kelvin, EIG, and WIG waves tend to have stronger relationship between $\lambda_{\overline{\omega}_{\text{mid}}}$ and $\lambda_{\delta r}$, suggesting that dynamical lifting of air, rather than column moisture, strongly influences the diurnal amplitude. Since the humidity profile of EIG and WIG is more tilted vertically, the same analysis is repeated with lower tropospheric specific humidity, integrated from 1000 to 600 hPa, which still did not show a strong linear relationship with $\lambda_{\delta r}$. These results suggest that the mechanism by which these waves interact with the diurnal cycle varies by the wave mode. For the MJO and ER, the evolutions of lower tropospheric horizontal wind, column humidity, and vertical motion are expected to be dynamically related. Therefore, in addition to the lower tropospheric wind speed, roles of thermodynamic variables such as column moisture must be considered to fully understand how large-scale disturbances interact with the diurnal cycle over the MC.

4. Discussion

Section 3a presented how the diurnal cycle evolves over the MC regions with the passages of the MJO and CCEWs. Although the relationship between the diurnal cycle and the MJO and CCEWs depends on the wave mode and geographical location, there are some consistent evolutions of cloud populations associated with changes in the diurnal amplitude and phase. Figure 14 illustrates the evolution of the diurnal cycle relative to

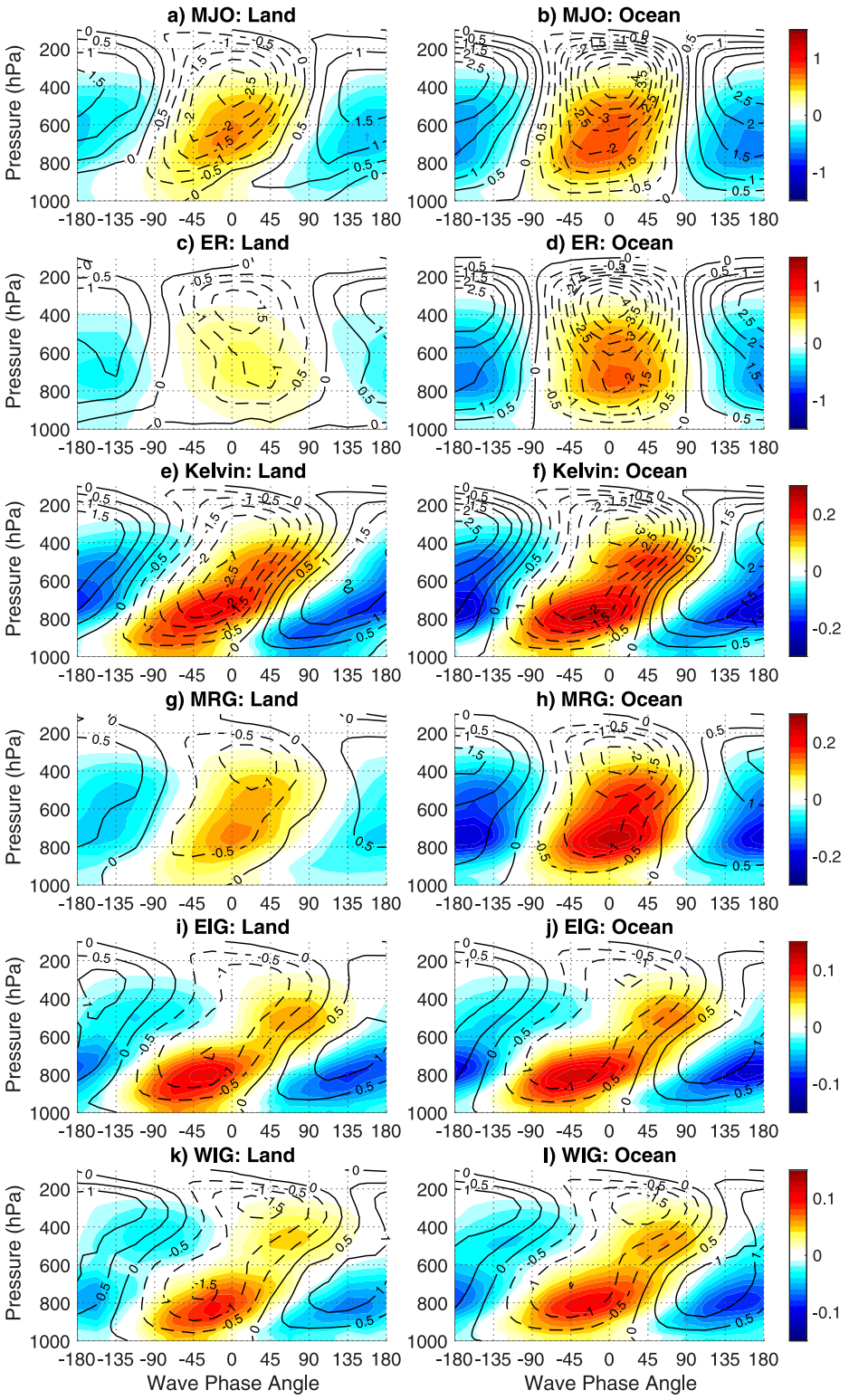

FIG. 12. Wave phase and pressure composites of specific humidity (shaded in g kg^{-1}) and pressure velocity (ω, contoured in hPa s^{-1}) over the land and ocean points within the Maritime Continent (0°N–12.5°S, 90°–165°E). The rows show the composites associated with the (a),(b) MJO, (c),(d) ER, (e),(f) Kelvin, (g),(h) MRG, (i),(j) EIG, and (k),(l) WIG.

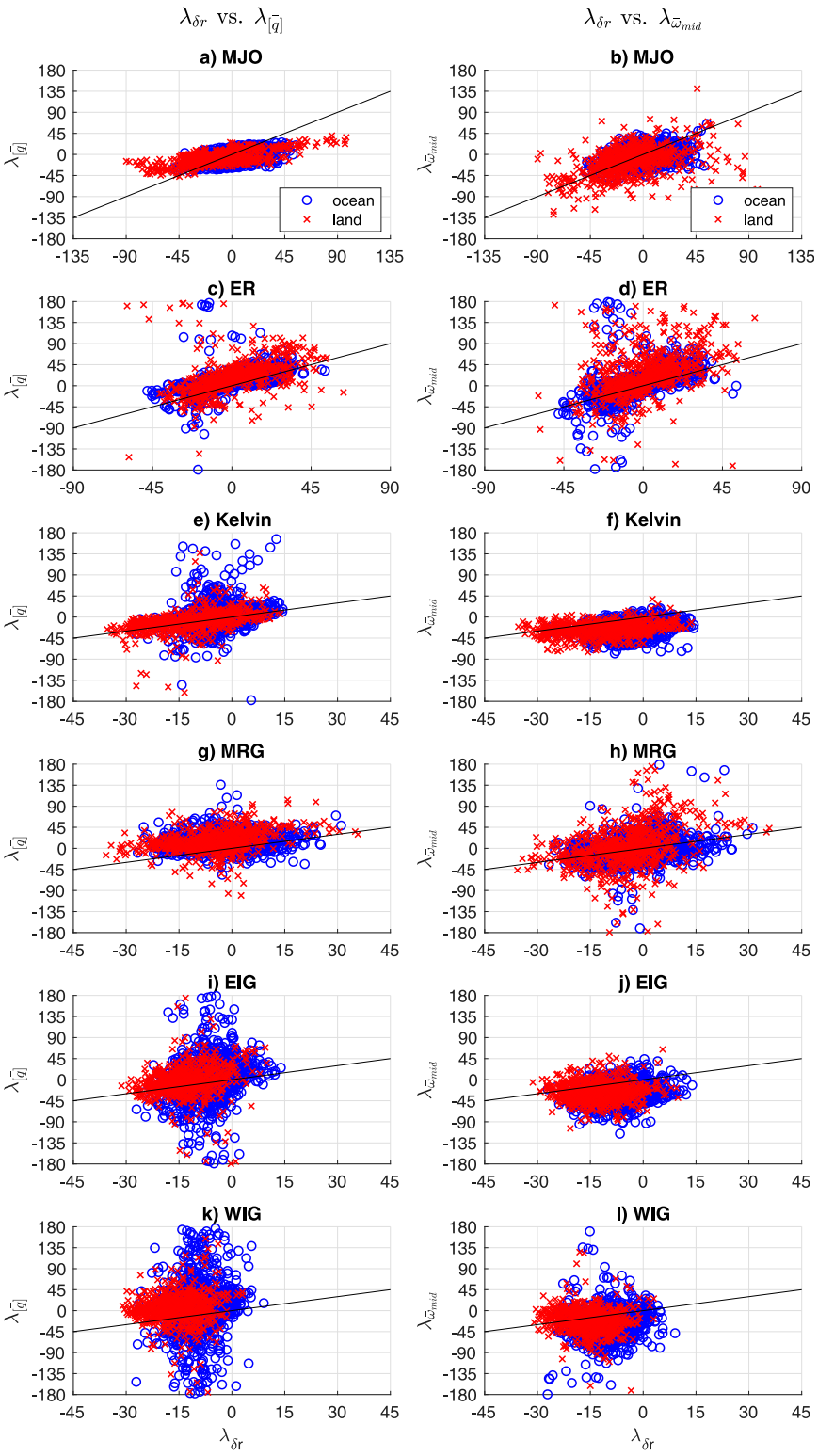

FIG. 13. (left) Wave phase at which the amplitude of the diurnal cycle peaks ($\lambda_{\delta r}$) plotted against wave phase at which the mass-weighted column-integrated (1000–200 hPa) specific humidity (kg kg^{-1} Pa) peaks ($\lambda_{[\bar{q}]}$), over land and ocean points of the MC region (0°N–12.5°S, 90°–165°E). (right) As in left, but $\lambda_{\delta r}$ is plotted against wave phase at which the mass-weighted midtropospheric (800–400 hPa) pressure velocity (hPa s^{-1}) peaks ($\lambda_{\bar{\omega}_{\mathrm{mid}}}$). The rows show the scatterplots of $\lambda_{\delta r}$,$\lambda_{[\bar{q}]}$, and $\lambda_{\bar{\omega}_{\mathrm{mid}}}$ of the (a),(b) MJO, (c),(d) ER, (e),(f) Kelvin, (g),(h) MRG, (i),(j) EIG, and (k),(l) WIG.

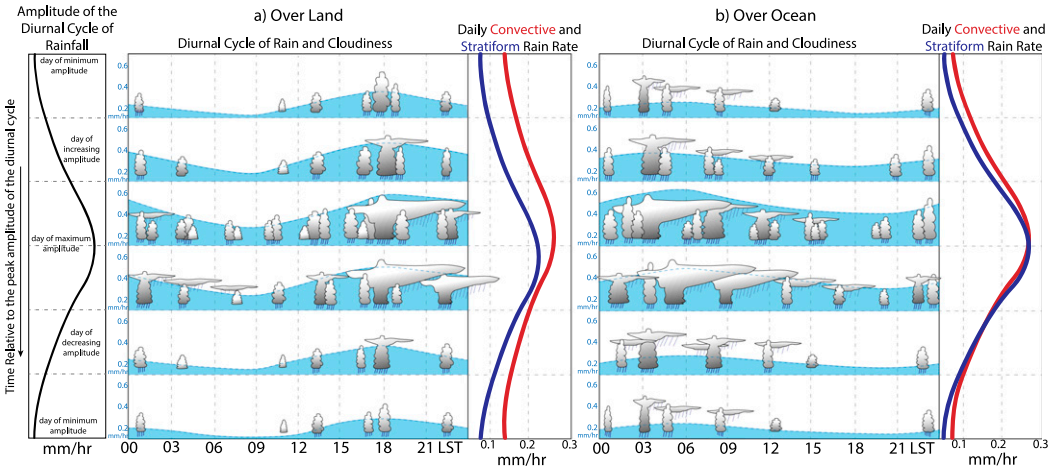

FIG. 14. Schematics of the evolution of the diurnal cycle of rainfall and cloudiness relative to the day of peak amplitude of the diurnal cycle associated with a passage of large-scale convective envelope over the Maritime Continent. Black line on the left shows the daily evolution of the amplitude of the diurnal cycle of total rainfall. The middle of the vertical axis indicates the day of peak amplitude of the diurnal cycle. (a) The diurnal cycle of total rainfall (blue shading) and associated cloud populations over land. The red and blue lines show the daily time series of convective and stratiform rain. (b) As in (a), but showing the diurnal cycle of rainfall over the surrounding oceanic area.

its day of peak diurnal amplitude over land and ocean. The black curve on the left shows the temporal evolution of the diurnal amplitude associated with the passage of a large-scale disturbance. The middle of the vertical axis denotes the day when the diurnal amplitude peaks. Over land, the peak diurnal amplitude occurs around the time when convective rainfall peaks. As shown in Fig. 10, convective rain dominates the total rainfall over land. The diurnal amplitude of convective rain is stronger than that of stratiform rain and there is a clear transition from a convective rainfall peak at 1500–1800 LST to a stratiform rain peak at 2100–2400 LST. Therefore, the diurnal amplitude of total rainfall increases the most when convective rain peaks before stratiform rain peaks. As cloud populations transition from convective to stratiform, the diurnal phase is delayed as stratiform rain extends the lifetime of organized clouds into morning hours. This extended and delayed life cycle of clouds also weakens the overall diurnal amplitude of rainfall. The diurnal amplitude continues to weaken as the suppressed convective envelope approaches.

Over the ocean, convective and stratiform rain contribute more equally to total rainfall, and there is a less clear separation of the diurnal cycle of convective and stratiform rainfall (Fig. 10). Therefore, the diurnal amplitude of total rainfall generally peaks when the total rainfall contributed by both convective and stratiform rain peaks. As stratiform rain becomes more dominant over convective rainfall over ocean, the diurnal phase is delayed by a few hours. In addition to the morning rainfall peak, previous studies have also identified the existence of the secondary peak in the afternoon (e.g., Ruppert and Johnson 2015; Sakaeda et al. 2018; Kerns and Chen 2018). The afternoon peak was not identified in this study using TRMM/GPM data, partly due to the use of the first 24-h harmonic to diagnose the diurnal cycle, since the afternoon peak often occurs as one of the weaker bimodal peaks. The lack of an afternoon peak in this study may also be due to our specific geographical focus over the MC, or some other limiting factors related to the detection of isolated shallow clouds in the afternoon by TRMM, as discussed by Sakaeda et al. (2018) and Kerns and Chen (2018). The general evolution of the diurnal amplitude and phase illustrated in Fig. 14 is further complicated by interactions between land–sea diurnal propagation of rain around the coastlines of the MC islands and how cloud populations are modulated by different wave modes.

Figure 15 illustrates changes in the propagation of diurnal rainfall along a mountainous coastline on days when a large-scale disturbance either strengthens or weakens the diurnal amplitude. On days when the diurnal amplitude is large (Fig. 15a), convection develops inland during the afternoon, which frequently organizes into a mesoscale convective system (Nesbitt and Zipser 2003). Rainfall then spreads downslope at a relatively faster speed, leading to an early onset of rainfall over coastal ocean that peaks in the early morning hours. Some rainfall continues to propagate offshore, peaking

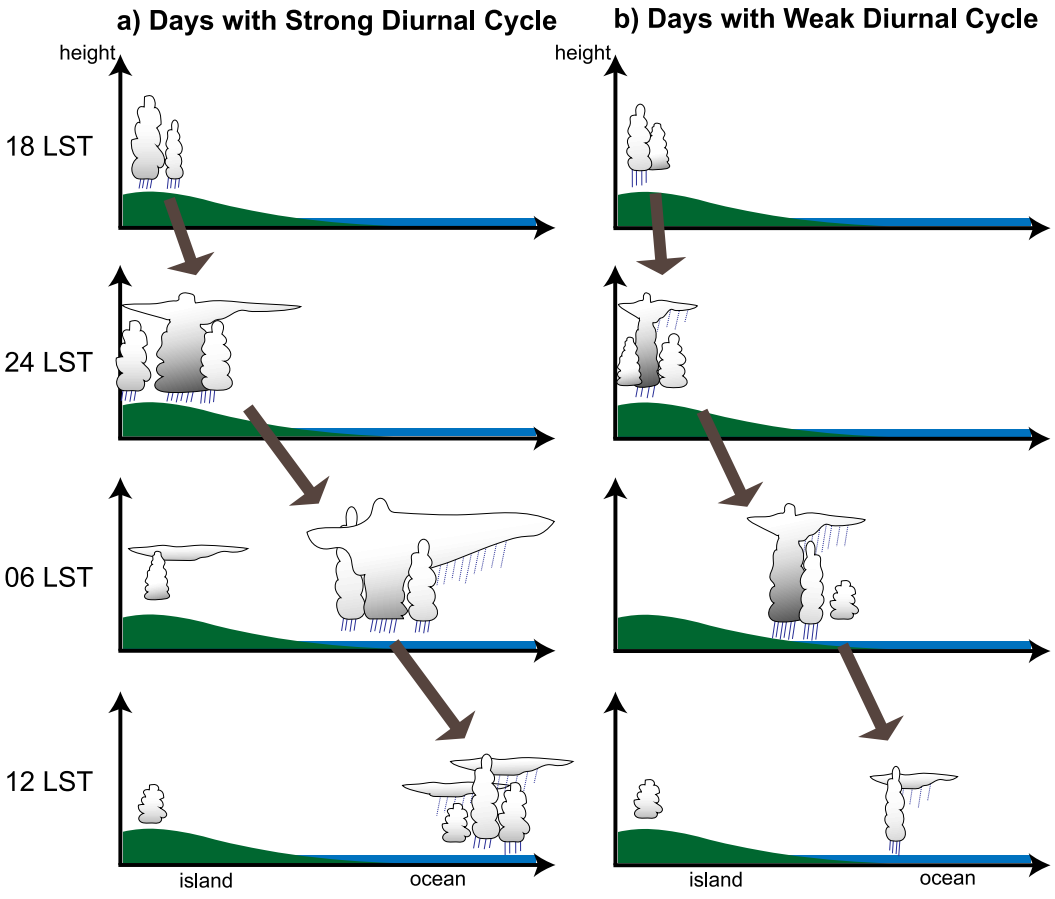

FIG. 15. Schematic of the diurnal propagation of clouds and rainfall from island mountainous areas toward offshore on days with (a) strong diurnal amplitude and (b) weak diurnal amplitude. Brown arrows represent the offshore propagation speed of rainfall.

in late morning to noon. On such days, the diurnal amplitude is strong over both landward and seaward sides of the coastline. The diurnal phase is then delayed over the islands due to the extended lifetime and horizontal extent of clouds as illustrated in Fig. 14a, while the diurnal phase is earlier over coastal ocean due to an earlier triggering of rainfall associated with the faster downslope propagation of rainfall. On days with weaker diurnal amplitude (Fig. 15b), convection that develops over inland areas does not intensify as much and propagates downslope at a slower speed or its propagation directions are more variable. On such days, the diurnal amplitude is weaker over both landward and seaward sides of the coastline, and the diurnal phase is earlier over inland areas due to the shorter lifetime of clouds, while the slower offshore propagation delays the diurnal phase over the coastal ocean.

The illustrated changes in the diurnal cycle of rainfall in Fig. 15 can occur asymmetrically or symmetrically across the terrain of MC islands. The MJO and ER waves tend to induce asymmetric modulation of the diurnal cycle, where the diurnal amplitude strengthens on one side (Fig. 15a) while weakening on the other side (Fig. 15b) of an island. This asymmetric modulation has been suggested to be mechanically forced by large-scale lower tropospheric wind anomalies (Qian 2008; Wang and Sobel 2017; Yanase et al. 2017), but section 3d showed that associated column moisture and large-scale vertical motion may play additional roles (Vincent and Lane 2017; Lu et al. 2019). Other faster-propagating waves (Kelvin, MRG, EIG, and WIG) tend to modulate the diurnal cycle more symmetrically around the islands (i.e., Figs. 15a or 15b on both sides of terrain), with the large-scale lower tropospheric wind seemingly playing a lesser role. The mechanism by which these waves modulate the diurnal cycle is still unclear, but column moisture or dynamically forced large-scale ascent is shown to have a strong relationship with the diurnal cycle, depending on the wave modes (Fig. 13). The changes in the land–sea propagation of rainfall could be

caused by changes in the intensity and propagation speed of gravity waves, land–sea breezes, vertical shear of lower tropospheric horizontal wind, or advection by large-scale flow (Mapes et al. 2003a; Qian 2008; Sakurai et al. 2009; Love et al. 2011; Hassim et al. 2016; Yanase et al. 2017; Yokoi et al. 2019). We find that the propagation speed of rainfall increases when inland convection is strong, which would theoretically induce a faster propagating gravity wave due to a longer vertical wavelength of heating (Yang and Slingo 2001; Mapes et al. 2003a; Beres et al. 2004). However, the roles of large-scale wind flow and moisture cannot be neglected as these effects can advect clouds (Yanase et al. 2017), mechanically force convection (Wang and Sobel 2017), and modulate gravity wave propagation speed through changing atmospheric stability and Doppler shifting (Mapes et al. 2003a).

5. Summary and conclusions

The Maritime Continent (MC) is characterized by highly varied topography and a strong diurnal cycle of rainfall that varies with the passage of large-scale disturbances. While many previous studies have focused on the relationship between the diurnal cycle and the MJO, only a limited number of studies have examined the relationship between the diurnal cycle and the CCEWs. This study uses TRMM and GPM data to understand how the diurnal cycle evolves differently within CCEWs compared to the MJO over the MC region. There are three main findings that resulted from this study. 1) The evolution of rain types (i.e., convective and stratiform) is tightly linked with changes in the diurnal amplitude and phase for all wave modes. 2) The evolution of rain types and the diurnal cycle associated with the MJO/CCEWs depend on geographical location and wave mode, with changes in the coastal land–sea propagation of diurnal rainfall being important for explaining the geographical dependency. 3) Rain types and the diurnal cycle are modulated by the MJO/CCEWs through different mechanisms associated with variations in moisture, vertical motion, and lower tropospheric wind perturbations.

For all the CCEWs and the MJO, their enhanced convective envelope generally leads to increased diurnal amplitude and a few hours of delay in the diurnal phase over both land and ocean. However, the exact timing of these changes relative to the center of the convective envelopes varies geographically (e.g., land versus ocean, and distance from coastlines) and by wave mode. Such changes in the diurnal amplitude and phase are also dependent on the evolution of cloud population, and thus the distribution of convective and stratiform rain, and land–sea diurnal propagation characteristics of rainfall. Over the islands, downslope and offshore propagation speed of rainfall from midnight to morning hours depends on the strength of convection, modulating the onset time of rainfall over coastal waters. We find that, for the MJO and ER waves, their lower tropospheric wind patterns play an important role in modulating the diurnal cycle over the MC islands. We also find that the evolution of rain type and the diurnal cycle with the waves over the MC is tightly linked to the evolution of tropospheric moisture profiles and vertical motion, except for EIG and WIG waves that seem to modulate the diurnal cycle through wind convergence rather than changes in column moisture. Modulation of moisture associated with the waves could be dynamically driven by large-scale circulation (e.g., through advection of moisture) or could be driven by the clouds themselves (e.g., through evaporation and cumulus moistening). Therefore, future studies investigating the causes of the differences in the evolution of tropospheric moisture among the MJO/CCEWs may help us better understand the two-way interactions of the waves and the diurnal cycle. Our study also did not investigate the modulation mechanism of land–sea diurnal propagation in detail, which remains as an open topic for future studies. In situ observations that have been and will be collected during the Year of Maritime Continent field campaign would provide valuable data to extend this type of analysis.

Acknowledgments. We thank Maria Gehne for her help in preparing part of the data used in this study. We thank the three anonymous reviewers for their helpful comments to significantly improve this manuscript. The TRMM and GPM data used in this study were obtained using the NASA Precipitation Processing System (PPS) FTP (https://pmm.nasa.gov/data-access/downloads). We gratefully acknowledge support for this work through Grant NA16OAR4320115 from the Climate Program Office at NOAA.

REFERENCES

Ahmed, F., and C. Schumacher, 2015: Convective and stratiform components of the precipitation–moisture relationship. *Geophys. Res. Lett.*, **42**, 10 453–10 462, https://doi.org/10.1002/2015GL066957.

Amante, C., and B. W. Eakins, 2009: ETOPO1 1 arc-minute global relief model: Procedures, data sources and analysis. NOAA Tech. Memo. NESDIS NGDC-24, 19 pp., ftp://ftp.library.noaa.gov/noaa_documents.lib/NESDIS/TM_NESDIS_NGDC/TM_NESDIS_NGDC_24.pdf.

Baranowski, D. B., M. K. Flatau, P. J. Flatau, and A. J. Matthews, 2016: Phase locking between atmospheric convectively coupled equatorial Kelvin waves and the diurnal cycle of precipitation over the Maritime Continent. *Geophys. Res. Lett.*, **43**, 8269–8276, https://doi.org/10.1002/2016GL069602.

Benedict, J. J., and D. A. Randall, 2007: Observed characteristics of the MJO relative to maximum rainfall. *J. Atmos. Sci.*, **64**, 2332–2354, https://doi.org/10.1175/JAS3968.1.

Bengtsson, L., and Coauthors, 2019: Convectively coupled equatorial wave simulations using the ECMWF IFS and the NOAA GFS cumulus convection schemes in the NOAA GFS model. *Mon. Wea. Rev.*, **147**, 4005–4025, https://doi.org/10.1175/MWR-D-19-0195.1.

Beres, J. H., M. J. Alexander, and J. R. Holton, 2004: A method of specifying the gravity wave spectrum above convection based on latent heating properties and background wind. *J. Atmos. Sci.*, **61**, 324–337, https://doi.org/10.1175/1520-0469(2004)061<0324:AMOSTG>2.0.CO;2.

Biasutti, M., S. E. Yuter, C. D. Burleyson, and A. H. Sobel, 2012: Very high resolution rainfall patterns measured by TRMM precipitation radar: Seasonal and diurnal cycles. *Climate Dyn.*, **39**, 239–258, https://doi.org/10.1007/s00382-011-1146-6.

Bretherton, C. S., J. R. McCaa, and H. Grenier, 2004: A new parameterization for shallow cumulus convection and its application to marine subtropical cloud-topped boundary layers. Part I: Description and 1D results. *Mon. Wea. Rev.*, **132**, 864–882, https://doi.org/10.1175/1520-0493(2004)132<0864:ANPFSC>2.0.CO;2.

Chen, S. S., and R. A. Houze, 1997: Diurnal variation and life-cycle of deep convective systems over the tropical Pacific warm pool. *Quart. J. Roy. Meteor. Soc.*, **123**, 357–388, https://doi.org/10.1002/qj.49712353806.

Dias, J., and G. N. Kiladis, 2016: The relationship between equatorial mixed Rossby-gravity and eastward inertio-gravity waves: Part II. *J. Atmos. Sci.*, **73**, 2147–2163, https://doi.org/10.1175/JAS-D-15-0231.1.

——, N. Sakaeda, G. N. Kiladis, and K. Kikuchi, 2017: Influences of the MJO on space–time organization of tropical convection. *J. Geophys. Res. Atmos.*, **122**, 8012–8032, https://doi.org/10.1002/2017JD026526.

——, M. Gehne, G. N. Kiladis, N. Sakaeda, P. Bechtold, and T. Haiden, 2018: Equatorial waves and the skill of NCEP and ECMWF numerical weather prediction systems. *Mon. Wea. Rev.*, **146**, 1763–1784, https://doi.org/10.1175/MWR-D-17-0362.1.

Fujita, M., K. Yoneyama, S. Mori, T. Nasuno, and M. Satoh, 2011: Diurnal convection peaks over the eastern Indian Ocean off Sumatra during different MJO phases. *J. Meteor. Soc. Japan*, **89A**, 317–330, https://doi.org/10.2151/jmsj.2011-A22.

Hagos, S. M., C. Zhang, Z. Feng, C. D. Burleyson, C. DeMott, B. Kerns, J. J. Benedict, and M. N. Martini, 2016: The impact of the diurnal cycle on the propagation of Madden–Julian oscillation convection across the Maritime Continent. *J. Adv. Model. Earth Syst.*, **8**, 1552–1564, https://doi.org/10.1002/2016MS000725.

Hassim, M. E. E., T. P. Lane, and W. W. Grabowski, 2016: The diurnal cycle of rainfall over New Guinea in convection-permitting WRF simulations. *Atmos. Chem. Phys.*, **16**, 161–175, https://doi.org/10.5194/acp-16-161-2016.

Henderson, D. S., C. D. Kummerow, D. A. Marks, and W. Berg, 2017: A regime-based evaluation of TRMM oceanic precipitation biases. *J. Atmos. Oceanic Technol.*, **34**, 2613–2635, https://doi.org/10.1175/JTECH-D-16-0244.1.

Hennon, C. C., and Coauthors, 2013: Tropical cloud cluster climatology, variability, and genesis productivity. *J. Climate*, **26**, 3046–3066, https://doi.org/10.1175/JCLI-D-12-00387.1.

Holloway, C. E., and J. D. Neelin, 2009: Moisture vertical structure, column water vapor, and tropical deep convection. *J. Atmos. Sci.*, **66**, 1665–1683, https://doi.org/10.1175/2008JAS2806.1.

Hou, A. Y., and Coauthors, 2014: The Global Precipitation Measurement Mission. *Bull. Amer. Meteor. Soc.*, **95**, 701–722, https://doi.org/10.1175/BAMS-D-13-00164.1.

Houze, R. A., Jr., K. L. Rasmussen, M. D. Zuluaga, and S. R. Brodzik, 2015: The variable nature of convection in the tropics and subtropics: A legacy of 16 years of the Tropical Rainfall Measuring Mission satellite. *Rev. Geophys.*, **53**, 994–1021, https://doi.org/10.1002/2015RG000488.

Huffman, G. J., and Coauthors, 2007: The TRMM Multisatellite Precipitation Analysis (TMPA): Quasi-global, multiyear, combined-sensor precipitation estimates at fine scales. *J. Hydrometeor.*, **8**, 38–55, https://doi.org/10.1175/JHM560.1.

Ichikawa, H., and T. Yasunari, 2006: Time–space characteristics of diurnal rainfall over Borneo and surrounding oceans as observed by TRMM-PR. *J. Climate*, **19**, 1238–1260, https://doi.org/10.1175/JCLI3714.1.

——, and ——, 2008: Intraseasonal variability in diurnal rainfall over New Guinea and the surrounding oceans during austral summer. *J. Climate*, **21**, 2852–2868, https://doi.org/10.1175/2007JCLI1784.1.

Iguchi, T., T. Kozu, R. Meneghini, J. Awaka, and K. Okamoto, 2000: Rain-profiling algorithm for the TRMM precipitation radar. *J. Appl. Meteor.*, **39**, 2038–2052, https://doi.org/10.1175/1520-0450(2001)040<2038:RPAFTT>2.0.CO;2.

Ikai, J., and K. Nakamura, 2003: Comparison of rain rates over the ocean derived from TRMM microwave imager and precipitation radar. *J. Atmos. Oceanic Technol.*, **20**, 1709–1726, https://doi.org/10.1175/1520-0426(2003)020<1709:CORROT>2.0.CO;2.

Inoue, K., and L. Back, 2015: Column-integrated moist static energy budget analysis on various time scales during TOGA COARE. *J. Atmos. Sci.*, **72**, 1856–1871, https://doi.org/10.1175/JAS-D-14-0249.1.

Janiga, M. A., C. J. Schreck, J. A. Ridout, M. Flatau, N. P. Barton, E. J. Metzger, and C. A. Reynolds, 2018: Subseasonal forecasts of convectively coupled equatorial waves and the MJO: Activity and predictive skill. *Mon. Wea. Rev.*, **146**, 2337–2360, https://doi.org/10.1175/MWR-D-17-0261.1.

Keenan, T. D., and R. E. Carbone, 2008: Propagation and diurnal evolution of warm season cloudiness in the Australian and Maritime Continent region. *Mon. Wea. Rev.*, **136**, 973–994, https://doi.org/10.1175/2007MWR2152.1.

Kerns, B. W., and S. S. Chen, 2014: ECMWF and GFS model forecast verification during DYNAMO: Multiscale variability in MJO initiation over the equatorial Indian Ocean. *J. Geophys. Res. Atmos.*, **119**, 3736–3755, https://doi.org/10.1002/2013JD020833.

——, and ——, 2018: Diurnal cycle of precipitation and cloud clusters in the MJO and ITCZ over the Indian Ocean. *J. Geophys. Res. Atmos.*, **123**, 10 140–10 161, https://doi.org/10.1029/2018JD028589.

Kikuchi, K., and B. Wang, 2008: Diurnal precipitation regimes in the global tropics. *J. Climate*, **21**, 2680–2696, https://doi.org/10.1175/2007JCLI2051.1.

Kiladis, G. N., M. C. Wheeler, P. T. Haertel, K. H. Straub, and P. E. Roundy, 2009: Convectively coupled equatorial waves. *Rev. Geophys.*, **47**, RG2003, https://doi.org/10.1029/2008RG000266.

——, J. Dias, and M. Gehne, 2016: The relationship between equatorial mixed Rossby–gravity and eastward inertio-gravity waves. Part I. *J. Atmos. Sci.*, **73**, 2123–2145, https://doi.org/10.1175/JAS-D-15-0230.1.

LeMone, M. A., E. J. Zipser, and S. B. Trier, 1998: The role of environmental shear and thermodynamic conditions in determining the structure and evolution of mesoscale convective systems

during TOGA COARE. *J. Atmos. Sci.*, **55**, 3493–3518, https://doi.org/10.1175/1520-0469(1998)055<3493:TROESA>2.0.CO;2.

Li, S., and A. W. Robertson, 2015: Evaluation of submonthly precipitation forecast skill from global ensemble prediction systems. *Mon. Wea. Rev.*, **143**, 2871–2889, https://doi.org/10.1175/MWR-D-14-00277.1.

Ling, J., C. Zhang, R. Joyce, P. Xie, and G. Chen, 2019: Possible role of the diurnal cycle in land convection in the barrier effect on the MJO by the Maritime Continent. *Geophys. Res. Lett.*, **46**, 3001–3011, https://doi.org/10.1029/2019GL081962.

Love, B. S., A. J. Matthews, and G. M. S. Lister, 2011: The diurnal cycle of precipitation over the Maritime Continent in a high-resolution atmospheric model. *Quart. J. Roy. Meteor. Soc.*, **137**, 934–947, https://doi.org/10.1002/qj.809.

Lu, J., T. Li, and L. Wang, 2019: Precipitation diurnal cycle over the Maritime Continent modulated by the MJO. *Climate Dyn.*, **53**, 6489–6501, https://doi.org/10.1007/s00382-019-04941-8.

Majda, A. J., and Q. Yang, 2016: A multiscale model for the intraseasonal impact of the diurnal cycle over the Maritime Continent on the Madden–Julian oscillation. *J. Atmos. Sci.*, **73**, 579–604, https://doi.org/10.1175/JAS-D-15-0158.1.

Mapes, B. E., T. T. Warner, and M. Xu, 2003a: Diurnal patterns of rainfall in northwestern South America. Part III: Diurnal gravity waves and nocturnal convection offshore. *Mon. Wea. Rev.*, **131**, 830–844, https://doi.org/10.1175/1520-0493(2003)131<0830:DPORIN>2.0.CO;2.

——, ——, ——, and A. J. Negri, 2003b: Diurnal patterns of rainfall in northwestern South America. Part I: Observations and context. *Mon. Wea. Rev.*, **131**, 799–812, https://doi.org/10.1175/1520-0493(2003)131<0799:DPORIN>2.0.CO;2.

Masunaga, H., T. Iguchi, R. Oki, and M. Kachi, 2002: Comparison of rainfall products derived from TRMM Microwave Imager and Precipitation Radar. *J. Appl. Meteor.*, **41**, 849–862, https://doi.org/10.1175/1520-0450(2002)041<0849:CORPDF>2.0.CO;2.

Matsuno, T., 1966: Quasi-geostrophic motions in the equatorial area. *J. Meteor. Soc. Japan*, **44**, 25–43, https://doi.org/10.2151/jmsj1965.44.1_25.

Mori, S., and et al, 2004: Diurnal land–sea rainfall peak migration over Sumatera Island, Indonesian Maritime Continent, observed by TRMM satellite and intensive rawinsonde soundings. *Mon. Wea. Rev.*, **132**, 2021–2039, https://doi.org/10.1175/1520-0493(2004)132<2021:DLRPMO>2.0.CO;2.

Neale, R., and J. Slingo, 2003: The Maritime Continent and its role in the global climate: A GCM study. *J. Climate*, **16**, 834–848, https://doi.org/10.1175/1520-0442(2003)016<0834:TMCAIR>2.0.CO;2.

Nesbitt, S. W., and E. J. Zipser, 2003: The diurnal cycle of rainfall and convective intensity according to three years of TRMM measurements. *J. Climate*, **16**, 1456–1475, https://doi.org/10.1175/1520-0442-16.10.1456.

Nguyen, H., and J.-P. Duvel, 2008: Synoptic wave perturbations and convective systems over equatorial Africa. *J. Climate*, **21**, 6372–6388, https://doi.org/10.1175/2008JCLI2409.1.

Oh, J.-H., K.-Y. Kim, and G.-H. Lim, 2012: Impact of MJO on the diurnal cycle of rainfall over the western Maritime Continent in the austral summer. *Climate Dyn.*, **38**, 1167–1180, https://doi.org/10.1007/s00382-011-1237-4.

Peatman, S. C., A. J. Matthews, and D. P. Stevens, 2014: Propagation of the Madden–Julian oscillation through the Maritime Continent and scale interaction with the diurnal cycle of precipitation. *Quart. J. Roy. Meteor. Soc.*, **140**, 814–825, https://doi.org/10.1002/qj.2161.

——, ——, and ——, 2015: Propagation of the Madden–Julian oscillation and scale interaction with the diurnal cycle in a high-resolution GCM. *Climate Dyn.*, **45**, 2901–2918, https://doi.org/10.1007/s00382-015-2513-5.

Qian, J.-H., 2008: Why precipitation is mostly concentrated over islands in the Maritime Continent. *J. Atmos. Sci.*, **65**, 1428–1441, https://doi.org/10.1175/2007JAS2422.1.

Rauniyar, S. P., and K. J. E. Walsh, 2011: Scale interaction of the diurnal cycle of rainfall over the Maritime Continent and Australia: Influence of the MJO. *J. Climate*, **24**, 325–348, https://doi.org/10.1175/2010JCLI3673.1.

Raupp, C. F. M., and P. L. Silva Dias, 2009: Resonant wave interactions in the presence of a diurnally varying heat source. *J. Atmos. Sci.*, **66**, 3165–3183, https://doi.org/10.1175/2009JAS2899.1.

Riley, E. M., B. E. Mapes, and S. N. Tulich, 2011: Clouds associated with the Madden–Julian oscillation: A new perspective from *CloudSat*. *J. Atmos. Sci.*, **68**, 3032–3051, https://doi.org/10.1175/JAS-D-11-030.1.

Ruppert, J. H., 2016: Diurnal timescale feedbacks in the tropical cumulus regime. *J. Adv. Model. Earth Syst.*, **8**, 1483–1500, https://doi.org/10.1002/2016MS000713.

——, and R. H. Johnson, 2015: Diurnally modulated cumulus moistening in the preonset stage of the Madden–Julian oscillation during DYNAMO. *J. Atmos. Sci.*, **72**, 1622–1647, https://doi.org/10.1175/JAS-D-14-0218.1.

——, and F. Zhang, 2019: Diurnal forcing and phase locking of gravity waves in the Maritime Continent. *J. Atmos. Sci.*, **76**, 2815–2835, https://doi.org/10.1175/JAS-D-19-0061.1.

Sakaeda, N., G. Kiladis, and J. Dias, 2017: The diurnal cycle of tropical cloudiness and rainfall associated with the Madden–Julian oscillation. *J. Atmos. Sci.*, **30**, 3999–4020, https://doi.org/10.1175/JCLI-D-16-0788.1.

——, S. W. Powell, J. Dias, and G. N. Kiladis, 2018: The diurnal variability of precipitating cloud populations during DYNAMO. *J. Atmos. Sci.*, **75**, 1307–1326, https://doi.org/10.1175/JAS-D-17-0312.1.

Sakurai, N., and Coauthors, 2005: Diurnal cycle of cloud system migration over Sumatera Island. *J. Meteor. Soc. Japan*, **83**, 835–850, https://doi.org/10.2151/jmsj.83.835.

——, and Coauthors, 2009: Internal structures of migratory cloud systems with diurnal cycle over Sumatera Island during CPEA-I campaign. *J. Meteor. Soc. Japan*, **87**, 157–170, https://doi.org/10.2151/jmsj.87.157.

Sui, C.-H., K.-M. Lau, Y. N. Takayabu, and D. A. Short, 1997: Diurnal variations in tropical oceanic cumulus convection during TOGA COARE. *J. Atmos. Sci.*, **54**, 639–655, https://doi.org/10.1175/1520-0469(1997)054<0639:DVITOC>2.0.CO;2.

Tabata, Y., H. Hashiguchi, M. K. Yamamoto, M. Yamamoto, M. D. Yamanaka, S. Mori, F. Syamsudin, and T. Manik, 2011: Observational study on diurnal precipitation cycle in equatorial Indonesia using 1.3-GHz wind profiling radar network and TRMM precipitation radar. *J. Atmos. Sol.-Terr. Phys.*, **73**, 1031–1042, https://doi.org/10.1016/j.jastp.2010.10.003.

Takayabu, Y. N., 1994: Large-scale cloud disturbances associated with equatorial waves. Part I: Spectral features of the cloud disturbances. *J. Meteor. Soc. Japan*, **72**, 433–449, https://doi.org/10.2151/jmsj1965.72.3_433.

——, and M. Murakami, 1991: The structure of super cloud clusters observed in 1–20 June 1986 and their relationship to easterly waves. *J. Meteor. Soc. Japan*, **69**, 105–125, https://doi.org/10.2151/jmsj1965.69.1_105.

Tian, B., D. E. Waliser, and E. J. Fetzer, 2006: Modulation of the diurnal cycle of tropical deep convective clouds by the MJO. *Geophys. Res. Lett.*, **33**, L20704, https://doi.org/10.1029/2006GL027752.

Tulich, S. N., and G. N. Kiladis, 2012: Squall lines and convectively coupled gravity waves in the tropics: Why do most cloud systems propagate westward? *J. Atmos. Sci.*, **69**, 2995–3012, https://doi.org/10.1175/JAS-D-11-0297.1.

Vincent, C. L., and T. P. Lane, 2017: A 10-year austral summer climatology of observed and modeled intraseasonal, mesoscale, and diurnal variations over the Maritime Continent. *J. Climate*, **30**, 3807–3828, https://doi.org/10.1175/JCLI-D-16-0688.1.

——, and ——, 2018: Mesoscale variation in diabatic heating around Sumatra, and its modulation with the Madden–Julian oscillation. *Mon. Wea. Rev.*, **146**, 2599–2614, https://doi.org/10.1175/MWR-D-17-0392.1.

——, ——, and M. C. Wheeler, 2016: A local index of Maritime Continent intraseasonal variability based on rain rates over the land and sea. *Geophys. Res. Lett.*, **43**, 9306–9314, https://doi.org/10.1002/2016GL069987.

Virts, K. S., J. M. Wallace, M. L. Hutchins, and R. H. Holzworth, 2013: Diurnal lightning variability over the Maritime Continent: Impact of low-level winds, cloudiness, and the MJO. *J. Atmos. Sci.*, **70**, 3128–3146, https://doi.org/10.1175/JAS-D-13-021.1.

Wang, S., and A. H. Sobel, 2017: Factors controlling rain on small tropical islands: Diurnal cycle, large-scale wind speed, and topography. *J. Atmos. Sci.*, **74**, 3515–3532, https://doi.org/10.1175/JAS-D-16-0344.1.

Wheeler, M. C., and G. Kiladis, 1999: Convectively coupled equatorial waves: Analysis of clouds in the wavenumber–frequency domain. *J. Atmos. Sci.*, **56**, 374–399, https://doi.org/10.1175/1520-0469(1999)056<0374:CCEWAO>2.0.CO;2.

——, ——, and P. J. Webster, 2000: Large-scale dynamical fields associated with convectively coupled equatorial waves. *J. Atmos. Sci.*, **57**, 613–640, https://doi.org/10.1175/1520-0469(2000)057<0613:LSDFAW>2.0.CO;2.

Yamanaka, M. D., S.-Y. Ogino, P.-M. Wu, J.-I. Hamada, S. Mori, J. Matsumoto, and F. Syamsudin, 2018: Maritime Continent coastlines controlling Earth's climate. *Prog. Earth Planet. Sci.*, **5**, 21, https://doi.org/10.1186/S40645-018-0174-9.

Yanase, A., K. Yasunaga, and H. Masunaga, 2017: Relationship between the direction of diurnal rainfall migration and the ambient wind over the southern Sumatra Island. *Earth Space Sci.*, **4**, 117–127, https://doi.org/10.1002/2016EA000181.

Yang, G.-Y., and J. Slingo, 2001: The diurnal cycle in the tropics. *Mon. Wea. Rev.*, **129**, 784–801, https://doi.org/10.1175/1520-0493(2001)129<0784:TDCITT>2.0.CO;2.

——, B. Hoskins, and J. Slingo, 2007: Convectively coupled equatorial waves. Part I: Horizontal and vertical structures. *J. Atmos. Sci.*, **64**, 3406–3423, https://doi.org/10.1175/JAS4017.1.

Yasunaga, K., and B. Mapes, 2012a: Differences between more divergent and more rotational types of convectively coupled equatorial waves. Part I: Space–time spectral analyses. *J. Atmos. Sci.*, **69**, 3–16, https://doi.org/10.1175/JAS-D-11-033.1.

——, and ——, 2012b: Differences between more divergent and more rotational types of convectively coupled equatorial waves. Part II: Composite analysis based on space–time filtering. *J. Atmos. Sci.*, **69**, 17–34, https://doi.org/10.1175/JAS-D-11-034.1.

Yokoi, S., S. Mori, M. Katsumata, B. Geng, K. Yasunaga, F. Syamsudin, Nurhayati, and K. Yoneyama, 2017: Diurnal cycle of precipitation observed in the western coastal area of Sumatra Island: Offshore preconditioning by gravity waves. *Mon. Wea. Rev.*, **145**, 3745–3761, https://doi.org/10.1175/MWR-D-16-0468.1.

——, ——, F. Syamsudin, U. Haryoko, and B. Geng, 2019: Environmental conditions for nighttime offshore migration of precipitation area as revealed by in situ observation off Sumatra Island. *Mon. Wea. Rev.*, **147**, 3391–3407, https://doi.org/10.1175/MWR-D-18-0412.1.